



A stochastic mathematical model of 4D tumour spheroids with real-time fluorescent cell cycle labelling

Jonah J. Klowss
BMath, BSc

Submitted in fulfilment
of the requirement for the degree of
Master of Philosophy (Mathematics)

School of Mathematical Sciences
Faculty of Science
Queensland University of Technology
2022

Keywords: Cancer; Melanoma; Individual-based model; FUCCI;
Population dynamics.

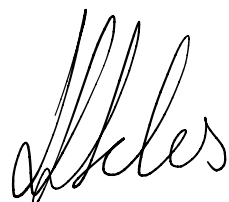
Statement of Original Authorship

In accordance with the requirements of the degree of Master of Philosophy (Mathematics) in the School of Mathematical Sciences, I present the following thesis entitled,

A stochastic mathematical model of 4D tumour spheroids with real-time fluorescent cell cycle labelling.

This work was performed under the supervision of Professor Matthew Simpson and Doctor Elliot Carr.

I declare that the work submitted in this thesis is my own, except as acknowledged in the text and footnotes, and has not been previously submitted for a degree at Queensland University of Technology or any other institution. To the best of my knowledge, no material in the thesis has been previously published or written by another person, with the exception of material duly referenced.



Jònah J. Klowss
May 12, 2022

Acknowledgements

Principally, I would like to extend my gratitude to my supervisors, Prof. Matthew Simpson and Dr. Elliot Carr. Your guidance, expertise and support throughout the course of this degree has been invaluable, and I am very grateful.

I would also like to extend my thanks to Mr. Ryan Murphy and Mr. Alex Browning. I very much appreciate your advice and assistance with computational and experimental work. To Prof. Nikolas Haass and Ms. Gency Gunasingh, I am grateful for your experimental expertise that has helped bring an additional dimension to this work. My gratitude also extends to Prof. Michael Plank, whose supervision of the mathematics and computational aspects of this work has been extremely helpful.

I acknowledge and thank the financial support provided by the Australian Research Council, and additionally the support provided by the School of Mathematical Sciences at QUT. I am also grateful to have had the opportunity to present this work at ANZIAM 2021.

Finally, I would like to extend my thanks to my family and friends. Your emotional support and encouragement throughout stressful and busy times helped this work to reach fruition.

Abstract

In vitro tumour spheroid experiments have been used to study avascular tumour growth and drug design for the last 50 years. Unlike simpler two-dimensional experiments, tumour spheroids lead to realistic heterogeneity within the growing population of cells that is thought to be related to spatial and temporal differences in nutrient availability. The relatively recent development of real-time fluorescent cell cycle labels allows us to identify the position of individual cells, as well as the cell cycle status of individual cells within the growing population, giving rise to the notion of a four-dimensional (4D) tumour spheroid. In this thesis, we develop the first stochastic individual-based model (IBM) of a 4D tumour spheroid and show that IBM simulation data compares very well with experimental data from a suite of 4D tumour spheroids constructed using a metastatic human melanoma cell line. Not only does the IBM replicate key qualitative features of the experiments, we also explore how the IBM provides quantitative information about nutrient availability within the spheroid, which is important because it is very difficult to measure these data in standard tumour spheroid experiments.

Contents

1	Introduction	1
1.1	Overview	1
1.1.1	Context	1
1.1.2	Fluorescent cell cycle labelling	4
1.1.3	Individual-based modelling	5
1.1.4	Research questions	6
1.2	Thesis structure	7
1.3	Statement of joint authorship	7
2	A stochastic mathematical model of 4D tumour spheroids	12
2.1	Introduction	12
2.2	Methods	15
2.2.1	Individual-based mathematical model	15
2.2.2	Simulation algorithm	19
2.2.3	IBM image processing	20
2.3	Results and Discussion	20
2.3.1	Parameter values	20
2.3.2	Qualitative comparison of experiments and simulations	22
2.3.3	Spheroid structure and nutrient profiles	24
2.3.4	Role of variability	27
2.3.5	Quantitatively matching experimental and mathematical spheroids	29
2.4	Conclusions and Future Work	31
3	Supporting information for a stochastic mathematical model of 4D tumour spheroids	33
3.1	Experimental methods	33
3.2	Image processing	34
3.3	Benchmarking the 3D numerical partial differential equation solution	40

3.4	Numerical method and parameters	42
3.4.1	Numerical discretisation	42
3.4.2	GMRES tolerance	42
3.4.3	Domain size	45
3.4.4	Spatial and temporal resolution of the nutrient profile	47
3.5	Estimation of cell diameter	50
3.6	Estimation of cell cycle progression rates	51
3.7	Initial cell number	53
3.8	Initialising the IBM	54
3.9	Simulation algorithms	56
3.10	Calculation of agent density profiles	58
3.11	Sensitivity analysis	61
3.11.1	Migration rates	61
3.11.2	Maximum death rate	62
3.11.3	Hill function index for arrest	62
3.12	Non-uniform nutrient delivery	66
3.13	Conclusion	70
4	Conclusion	72
4.1	Summary	72
4.2	Discussion	73
4.3	Future Work	74
	Bibliography	76

List of Figures

1.1	3D cell culture experiments	2
1.2	Growth of a tumour spheroid	3
1.3	Fluorescent cell cycle labelling schematic	4
2.1	Model motivation	13
2.2	Schematic of the IBM	16
2.3	Comparison of <i>in vitro</i> and <i>in silico</i> spheroids	23
2.4	Spheroid structure	25

2.5	Nutrient concentration profiles	26
2.6	Hypoxia staining	28
2.7	Spheroid population profiles with variability	29
2.8	Quantitatively matching experiments and simulations	30
3.1	Outer and necrotic radius estimates	35
3.2	Arrest radius estimates	39
3.3	Numerical discretisation benchmarking	41
3.4	Variation of initial accuracy of GMRES	43
3.5	Variation of accuracy in subsequent GMRES solutions	45
3.6	Effect of domain length	45
3.7	Spatial and temporal resolution 1	46
3.8	Spatial and temporal resolution 2	48
3.9	Estimating the cell diameter	50
3.10	Estimating time spent in cell cycle phases	51
3.11	Population estimates at spheroid formation	52
3.12	Initialising the agent cycling status in the model	55
3.13	Agent density profile demonstration	59
3.14	Model sensitivity to movement rate	61
3.15	Model sensitivity to death rate	62
3.16	Model sensitivity to Hill index for arrest	63
3.17	Effect of Hill index on qualitative spheroid growth	64
3.18	Non-uniform nutrient delivery at 0 days	67
3.19	Non-uniform nutrient delivery at 3 days	68
3.20	Non-uniform nutrient delivery at 6 days	69
3.21	Non-uniform nutrient delivery at 10 days	70

Chapter 1

Introduction

1.1 Overview

1.1.1 Context

Tumour spheroids are a valuable experimental tool for studying the dynamics of *in vivo* tumours. The relevance of tumour spheroid experiments is due to how they physiologically mimic the structural and temporal heterogeneity of solid tumours to a degree unmatched by two dimensional (2D) cell culture experiments [1–3] (Figure 1.1), where nutrient is freely available above the monolayer of cells (Figure 1.1c). In tumour spheroids, the three dimensional spatial structure limits the diffusion of nutrient, causing a gradient of nutrient availability (Figure 1.1c). In addition, tumour spheroid experiments respond to the influence of anticancer drugs and nutrient deprivation in a manner reminiscent of that exhibited by tumours *in vivo* [2, 4, 5]. Hence, tumour spheroids are experimental assays that are valuable intermediates between 2D cell culture experiments and live-tissue animal models [6].

Tumour spheroids begin as cells suspended in a growth medium, which aggregate themselves together over time, forming a spheroid which then begins growing [2, 7]. Once a spheroid reaches approximately 300-400 μm in diameter, the cells in the centre become quiescent and arrest their progression through the cell cycle, and stop proliferating, as a response to reduced access to nutrient [7, 8]. Further growth causes the spheroid, with its centre even more restricted from access to nutrient, to begin developing a necrotic core, region of reduced proliferation, and freely proliferating periphery in a concentric structure [7–9]. The three dimensions of spatial growth and

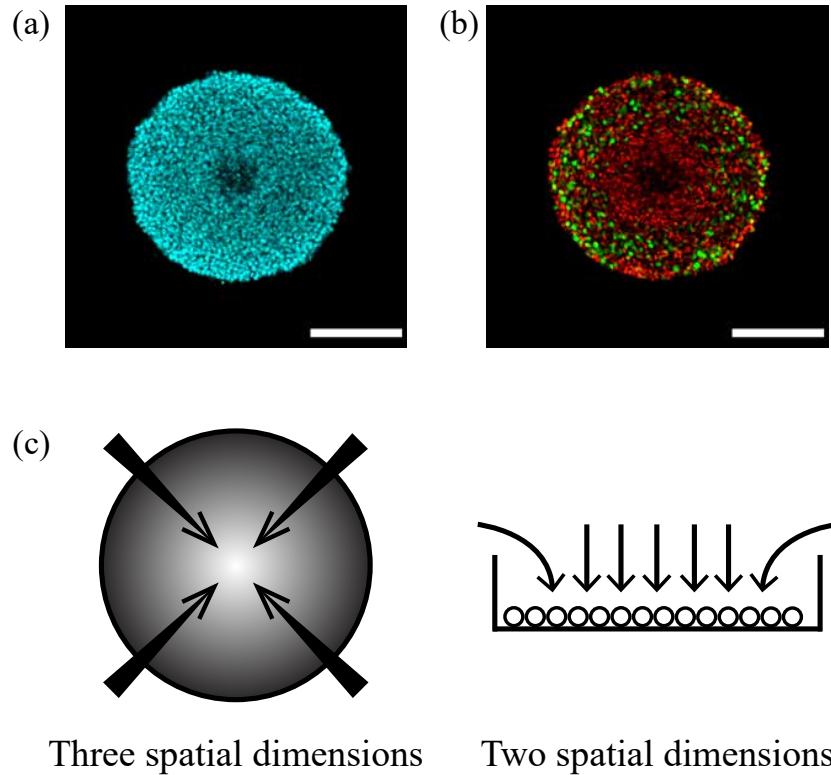


Figure 1.1: Advantages of tumour spheroid experiments. (a)–(b) Comparison of spheroids with and without cell cycle status labels. Images show (a) cell nuclei and (b) cell nuclei exhibiting fluorescence indicating the cell cycle status of each cell. (c) Schematic comparison of tumour spheroid experiments (left) and 2D cell cultures (right) with nutrient (arrows).

additional information about the individual cell cycle status of each cell (Figure 1.1b) gives rise to the terminology of a *4D tumour spheroid*. Figure 1.2 demonstrates this spheroid growth and internal heterogeneity in a human melanoma cell line over a 6 day period.

The study of these tumour spheroids is an important field in mathematical oncology [9]. Continuum mathematical models aiming to describe the formation and growth phases of internal spheroid structure were first developed over 50 years ago [9, 10]. Modelling of tumour spheroids has since been further developed and analysed to model nutrient diffusion into the spheroid, necrotic core growth, and the formation of quiescent regions [11–17]. Continuum models describe the spheroid as a continuum of cells, where partial differential equations govern nutrient concentrations and cell migration, proliferation and death [18].

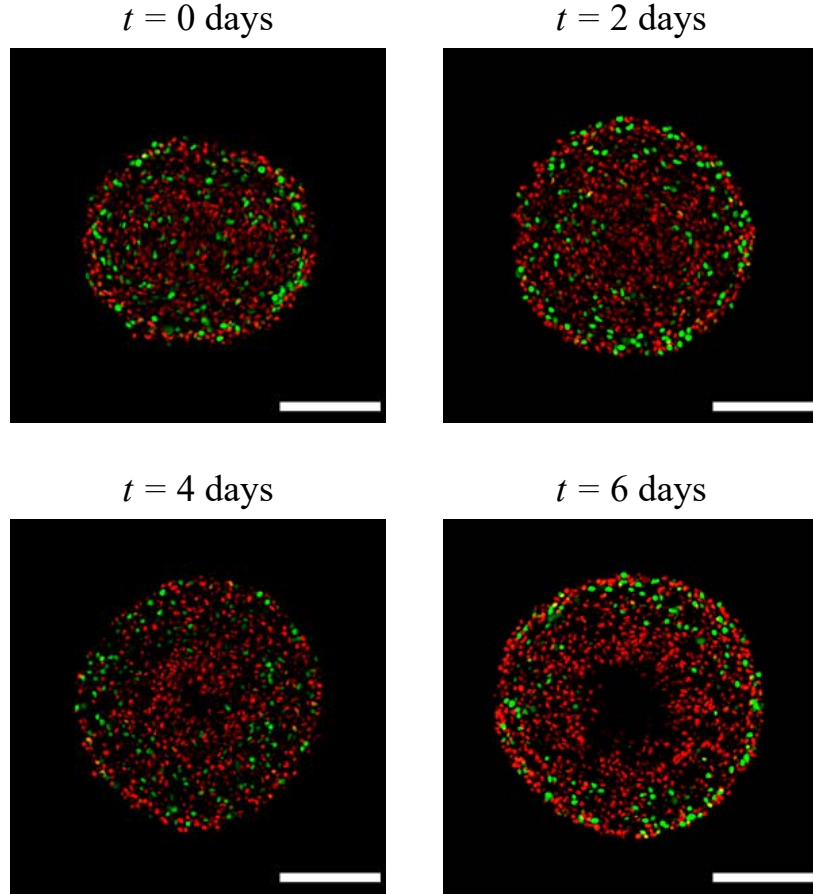


Figure 1.2: Cross section images of a tumour spheroid demonstrating structural growth at $t = 0, 2, 4$, and 6 days. Different colours indicate cells in different stages of the cell cycle, and the absence of fluorescence in the centre at $t = 6$ days is the region of the necrotic core. Scale bars represent $200 \mu\text{m}$.

In this thesis, we will take a different approach by considering the tumour spheroids as a conglomeration of individual cells, with an evolution arising from the collective behaviour of cells and their interaction with their environment, such as nutrient availability. This modelling approach will be connected with new experiments performed for this thesis. In Figure 1.2, we see cells at an individual resolution via the indication of their cell cycle statuses. Hence, the opportunity to model the spheroid and its evolution by considering individual cell behaviours and properties, including cell cycle indicators, arises.

1.1.2 Fluorescent cell cycle labelling

Until 2008, individual cell cycle status data were obscured from cell culture assays, with no means of explicitly distinguishing the cycling phases of individual cells [19]. However, the advent of *fluorescent ubiquitination-based cell cycle indicator* (FUCCI) technology has enabled the identification of the cell cycle status of individual cells with fluorescent sensors [5, 19, 20]. With FUCCI, cell nuclei in gap 1 (G1) phase fluoresce red, and cell nuclei in the synthesis/gap 2/mitosis (S/G2/M) phase fluoresce green (Figure 1.3). When cell nuclei are in early S (eS) phase, they emit both colours, and appear yellow [19]. A significant application of cell cycle labelling is explicitly indicating regions where cells are arrested in G1 phase and therefore not cycling and proliferating. This may be natural, as a consequence of low nutrient availability [7, 8], or from the inclusion of drugs that rely on impeding or disrupting the cell cycle [4, 5].

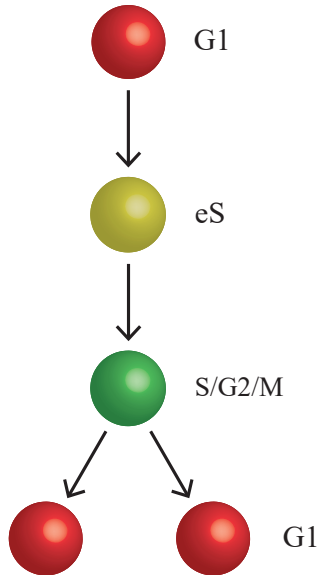


Figure 1.3: Schematic of *fluorescent ubiquitination-based cell cycle indicator* (FUCCI) technology on cycling cells. Cell nuclei fluoresce red when in G1 phase, yellow when in eS phase, and green in S/G2/M phase.

Just as FUCCI labelling enables experimentalists to see additional cell cycle status details, so too can modellers see greater detail in models with collective cell behaviour. While there are mathematical models of tumour spheroids and cell cultures with proliferation without FUCCI labelling [21–24], other models have implemented cell cycle labelling mechanisms with

success. Some models have used FUCCI labelling in continuous models of tumour spheroid experiments [25, 26], whereas others explicitly label the cell cycle status of individual cells in 2D cell culture experiments [20, 27–30]. In this thesis, we consolidate these approaches by explicitly indicating the cycling status of individual cells in a mathematical model of tumour spheroid experiments.

1.1.3 Individual-based modelling

Individual-based models (IBMs) are a class of discrete model simulations that describe systems as comprised of collections of individuals whose behaviours are influenced by their state variables. This kind of approach can have substantial utility in a biological context, where individual-level information can be highly heterogeneous [31]. These models have been applied with great success to modelling collective cell behaviour in 2D [21, 22, 32, 33], where the behaviour of individual cells is responsible for the overall evolution of the system. Individual-based models, like most discrete models, can be less computationally efficient than continuum models [18]. IBMs overcome this disadvantage of increased computational workload by often being a highly appropriate choice for the biology being modelled [21, 22, 32], or by simply relaying more detailed information at the individual level than a continuous model can.

A key difference between assays with two spatial dimensions and tumour spheroid experiments is the spatial variation in nutrient availability. Tumour spheroid experiments have the additional restriction on local nutrient availability for cells in the spheroid centre; once the spheroid exceeds a certain size, it is larger than the diffusion limit for nutrients [7–9], and cells in the centre are deprived of nutrient necessary for cell cycling or even survival [5, 34]. Because of this feature of 3D experiments that isn't present in 2D assays, we must also consider the reaction-diffusion (consumption-diffusion) of nutrient, and the relationship between nutrient concentration and cell behaviours, such as committing to the cell cycle, cell migration, and cell death.

If the information on the individual cell level is of interest, then IBMs are the most suitable approach. Some IBMs of tumour spheroid growth have been developed, where individual cells are classified based on their local oxygen level and entry into a quiescent or necrotic state [23, 24, 35]. However, cell cycle indicators (see Section 1.1.2) are uniquely suited individual-

based approaches, as they naturally assign each individual cell an additional state variable – its cell cycle status. Since much of the spatial heterogeneity is hypothesized to be driven by arrest of the cell cycle, we are motivated to explicitly include cell cycle indicators into a mathematical model to investigate these dynamics. In this thesis, we aim to consolidate IBMs of 4D tumour spheroids with IBMs explicitly modelling the cell cycle, taking advantage of directly modelling cell cycle labelling with FUCCI and cell death, which has the added benefit of direct comparisons between our model results with those from experiments.

As many mathematical models are developed with the intention of replicating experimental phenomena, the utilisation of experimental data is central to verifying these models. As such, since IBMs may utilise and impart the same cell-level information as the experimental counterparts, they are a strong choice for modelling biological phenomena, as an IBM's fidelity can be directly compared to the experimental data [31]. It is for this reason that, in this thesis, we place significant emphasis on how measurements from the model compare with experimental results. We can then use the model to extract data that are obscured in experiments, after demonstrating that the simulation is a viable representation of the experimental growth of a 4D tumour spheroid with cell cycle labelling.

1.1.4 Research questions

In this thesis, we aim to address the following research questions:

1. How can previous techniques used in cell population dynamics and cell cycle labelling be extended to three dimensions?
2. How do individual-based models of tumour spheroid growth compare with experimental images of tumour spheroids grown *in vitro*?
3. What insight can an individual-based model of tumour spheroid growth provide into information normally obscured in experiments?

In answering these questions, the methods in previous studies are consolidated and extended, and the spatial and temporal evolution of 4D tumour spheroids is investigated.

1.2 Thesis structure

This thesis contains two main chapters. In Chapter 2, we include the main document of a scientific manuscript submitted to the *Journal of the Royal Society Interface* (November 2020). In Chapter 3, we present the supplementary material supporting the manuscript in Chapter 2. Both the manuscript and supplementary material are available on bioRxiv, at <https://www.biorxiv.org/content/10.1101/2021.11.28.470300v1>. Software and code required to implement the IBM is also available on GitHub, at <https://github.com/ProfMJSimpson/4DFUCCI>.

Chapter 2 presents a continuous-space, continuous-time individual-based model of 4D tumour spheroid growth with fluorescent cell cycle indicators. Individual cell migration, death, and proliferation are explicitly described in the context of a 4D tumour spheroid, and biological inspiration is used to model how the local nutrient concentration influences these behaviours. Qualitatively comparing the results of the IBM with experiments demonstrates its biological fidelity, and quantitative data is then extracted from the IBM. Using a careful selection of parameter values, the quantitative experimental behaviour of experimental spheroids is matched with the IBM.

In Chapter 3, the numerical methods for the individual-based model and coupled reaction-diffusion equation utilised in Chapter 2 are described. A series of computational experiments justifying the selection of numerical parameter choices for the solution of the reaction-diffusion equation are also presented. The calculations of experimentally supported parameters, with an overview of the associated experimental method to achieve them, are also outlined in Chapter 3. The methodology and pseudo-code for the IBM and reaction-diffusion equation are also included.

In Chapter 4, we summarise this thesis and its key findings, and outline possible avenues for extending this research.

1.3 Statement of joint authorship

This section outlines the joint contributions of the Masters candidate and the co-authors of the scientific manuscript and supporting material presented in this thesis.

Chapter 2: A stochastic mathematical model of 4D tumour spheroids

This chapter is the main document of the manuscript titled “A stochastic mathematical model of 4D tumour spheroids with real-time fluorescent cell cycle labelling”. This manuscript is publicly available on [bioRxiv](#), and has been submitted for publication in the *Journal of the Royal Society Interface* (November 2020). Below, the contribution of each author is listed:

- Jonah J. Klowss developed the IBM, performed all numerical simulations, performed all experiments, analysed the simulation and experimental data, generated the figures, and drafted the manuscript,
- Alexander P. Browning assisted with numerical simulations, assisted with experimental work, supervised the data analysis and figure generation, and critically reviewed the manuscript.
- Ryan J. Murphy assisted with numerical simulations, assisted with experimental work, and critically reviewed the manuscript.
- Elliot J. Carr supervised the numerical simulations, data analysis, and figure generation, and critically reviewed the manuscript.
- Michael J. Plank supervised the data analysis and figure generation, and critically reviewed the manuscript.
- Gency Gunasingh instructed and supervised the experimental work, supervised the experimental data analysis and figure generation, and critically reviewed the manuscript.
- Nikolas K. Haass supervised the experimental work, experimental data analysis and figure generation, and critically reviewed the manuscript.
- Matthew J. Simpson initiated the research concept, supervised the numerical simulations, data analysis, and figure generation, and critically reviewed the manuscript.

Chapter 3: Supporting information for a stochastic mathematical model of 4D tumour spheroids

This chapter is the supplementary material document for the manuscript titled “A stochastic mathematical model of 4D tumour spheroids with real-

time fluorescent cell cycle labelling”, which comprises Chapter 2. Below, the contribution of each author is listed:

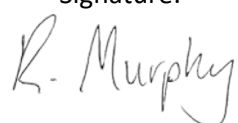
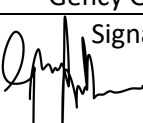
- Jonah J. Klowss developed the mathematical techniques, performed the analysis and supplementary experiments, generated the figures, and drafted the manuscript.
- Alexander P. Browning supervised the data analysis and figure generation, and critically reviewed the manuscript.
- Ryan J. Murphy critically reviewed the manuscript.
- Elliot J. Carr supervised the mathematical techniques, data analysis, and figure generation, and critically reviewed the manuscript.
- Michael J. Plank supervised the mathematical techniques, data analysis and figure generation, and critically reviewed the manuscript.
- Gency Gunasingh instructed and supervised the supplementary experimental work, supervised the experimental data analysis and figure generation, and critically reviewed the manuscript.
- Nikolas K. Haass supervised the supplementary experimental work, experimental data analysis and figure generation, and critically reviewed the manuscript.
- Matthew J. Simpson supervised the mathematical techniques, data analysis, and figure generation, and critically reviewed the manuscript.

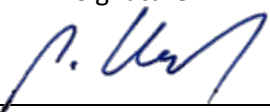
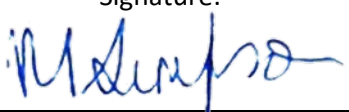
The authors listed below have certified that:

1. they meet the criteria for authorship in that they have participated in the conception, execution, or interpretation, of at least that part of the publication in their field of expertise;
2. they take public responsibility for their part of the publication, except for the responsible author who accepts overall responsibility for the publication;
3. there are no other authors of the publication according to these criteria;
4. potential conflicts of interest have been disclosed to (a) granting bodies, (b) the editor or publisher of journals or other publications, and (c) the head of the responsible academic unit, and
5. they agree to the use of the publication in the student's thesis and its publication on the QUT's ePrints site consistent with any limitations set by publisher requirements.

Publication title: A stochastic mathematical model of 4D tumour spheroids with real-time fluorescent cell cycle labelling

Publication status: Submitted to Journal of the Royal Society Interface

Jonah J. Klowss Signature: 	Date: 06/12/2021	Developed the IBM, performed all numerical simulations, performed all experiments, analysed the simulation and experimental data, generated the figures, and drafted the manuscript.
Alexander P. Browning Signature: 	Date: 6 Dec 2021	Assisted with numerical simulations, assisted with experimental work, supervised the data analysis and figure generation, and critically reviewed the manuscript.
Ryan J. Murphy Signature: 	Date: 6 Dec 2021	Assisted with numerical simulations, assisted with experimental work, and critically reviewed the manuscript.
Elliot J. Carr Signature: 	Date:	Supervised the numerical simulations, data analysis, and figure generation, and critically reviewed the manuscript.
Michael J. Plank Signature:	Date:	Supervised the data analysis and figure generation, and critically reviewed the manuscript
Gency Gunasingh Signature: 	Date: 7 Dec 2021	Instructed and supervised the experimental work, supervised the experimental data analysis and figure generation, and critically reviewed the manuscript.

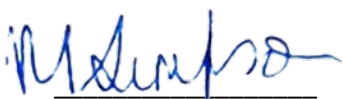
Nikolas Haass	
Signature:	Supervised the experimental work, experimental data analysis and figure generation, and critically reviewed the manuscript.
	
Date:	
Matthew J. Simpson	
Signature:	Initiated the research concept, supervised the numerical simulations, data analysis, and figure generation, and critically reviewed the manuscript.
	
Date:	

Principal supervisor confirmation

I have sighted email or other correspondence from all Co-authors confirming their certifying authorship. (If the Co-authors are not able to sign the form please forward their email or other correspondence confirming the certifying authorship to the RSC).

Professor Matthew Simpson

Name



Signature

7/12/2021

Date

Chapter 2

A stochastic mathematical model of 4D tumour spheroids

2.1 Introduction

In vitro tumour spheroid experiments are widely-adopted to study avascular tumour growth and anti-cancer drug design [1–3]. Unlike simpler two-dimensional assays, tumour spheroid experiments exhibit heterogeneity within the growing population of cells, and this heterogeneity is thought to be partly driven by spatial and temporal differences in the availability of diffusible nutrients, such as oxygen [2,5]. Historically, tumour spheroids have been analysed experimentally using bright field imaging to measure the size of the growing spheroid [8, 36], however this approach does not reveal information about the internal structure of the growing population. Since 2008, *fluorescent ubiquitination-based cell cycle indicator* (FUCCI) has enabled real-time identification of the cell cycle for individual cells within growing populations [5, 19, 20]. Using FUCCI, nuclei of cells in G1 phase fluoresce red, nuclei of cells in S/G2/M phase fluoresce green, and nuclei of cells in early S (eS) phase appear yellow as a result of both red and green fluorescence being active [19] (Figure 2.1a). FUCCI simultaneously provides information about spheroid size and heterogeneity of the cell cycle status (Figure 2.1c-e). In particular, at early times the entire spheroid is composed of freely cycling cells, with a relatively even distribution of FUCCI colours, whereas at intermediate times cells in the central region

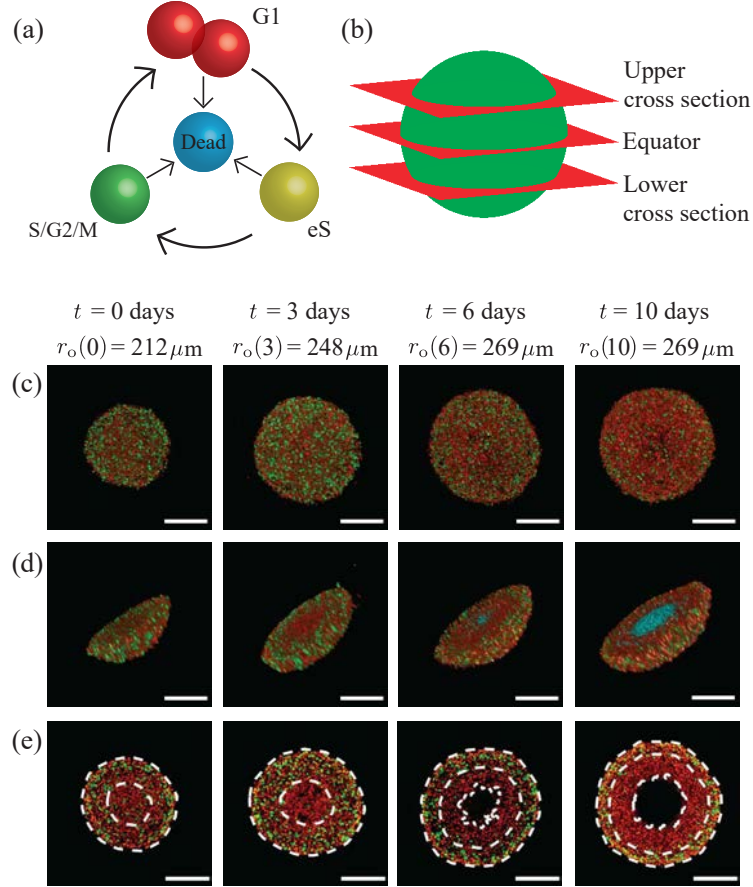


Figure 2.1: Motivation. (a) A schematic of the cell cycle, indicating the transition between different cell cycle phases, and their associated FUCCI fluorescence. Red, yellow, and green colouring indicates cells in G1, eS, and S/G2/M phase, respectively. (b) Locations of the upper cross section, equator and lower cross section. (c)–(e) Experimental images of a tumour spheroid using the human melanoma cell line WM793B at days 0, 3, 6, and 10 (after formation) showing: (c) full spheroids, viewed from above; (d) spheroid hemispheres; and, (e) spheroid slices, where the cross section is taken at the equator. White dashed lines in (e) denote the boundaries of different regions, where the outermost region is the proliferative zone, the next region inward is the G1-arrested region, and the innermost region at days 6 and 10 is the necrotic core. In (a) and (d) we use cyan colouring for dead cells, which assist in identifying the necrotic core in (d), where the cyan fluorescence is from experimental necrosis staining with DRAQ7 (Section 3.1). Spheroid outer radii are labelled alongside their corresponding time points, and scale bars represent 200 μm .

become predominantly red, indicating G1-arrest [5]. Late time growth is characterised by the formation of a central necrotic region, indicated by a

complete absence of fluorescence. FUCCI allows us to identify both the position of individual cells within the growing spheroid in three spatial dimensions, as well as identifying cell cycle status, giving rise to the notion of a *four-dimensional (4D) tumour spheroid* [25]. Assuming spherical symmetry, we can characterise the geometry of 4D spheroids by three radii: $r_o(t) > 0$ is the outer radius, $r_a(t) \geq 0$ is the arrested radius, and $r_n(t) \geq 0$ is the necrotic radius, with $r_o(t) > r_a(t) \geq r_n(t)$. In Figure 2.1e, we see that $r_n(t) = 0$ for $t \leq 3$, with the necrotic core forming sometime between $t = 3$ and $t = 6$ days.

Continuum mathematical models of tumour spheroids have been developed, analysed, and deployed for over 50 years [10–12, 16, 17, 37], and these developments have included very recent adaptations of classical models to study tumour spheroids with FUCCI [25, 26, 38]. Continuum modelling approaches lack the ability to track individual cells within the growing population, and typically neglect heterogeneity and stochasticity. In comparison, individual-based models (IBMs) allow us to study population dynamics in more detail, by keeping track of all individuals and explicitly capturing heterogeneity and stochasticity [30, 39]. Over the last 20 years, as computing power has increased at the same time that experimental imaging resolution has improved, there has been an increasing interest in interpreting tumour spheroid experiments using IBMs [23, 24, 40–43], with some studies using these models to focus explicitly on how the balance of cell migration and cell proliferation impacts phenotype selection [44]. Flegg and Nataraj (2019) succinctly review mathematical modelling methodologies used to interpret tumour spheroid experiments [45]. While several previous IBMs have the ability to track the cell cycle within individuals [23, 24, 40–43], our aim is to track the cell cycle in a relatively minimal IBM and to quantitatively interpret this information in terms of a new set of 4D tumour spheroid experiments.

In this work, we develop a continuous-space, continuous-time IBM of 4D tumour spheroid growth with FUCCI. The IBM explicitly describes how individual cells migrate, die, and progress through the cell cycle to mimic FUCCI. Certain mechanisms in the IBM are coupled to the local availability of a diffusible nutrient. We demonstrate the biological fidelity of the IBM by qualitatively comparing simulation results with detailed experimental images at several cross sections (Figure 2.1b), with the aim of providing more comprehensive detail about the internal structure. Quantitative data from the model are then used to assess the spheroid population

distribution, nutrient concentration, and the role variability plays in the spheroid. We extract and quantitatively compare simulation radius estimates with measurements from a series of 4D tumour spheroid experiments using a human primary melanoma cell line (Figure 2.1). Using a careful choice of parameter values, we also show that the IBM quantitatively replicates key features of 4D tumour spheroids.

2.2 Methods

Experimental methods are described in Section 3.1.

2.2.1 Individual-based mathematical model

We simulate 4D spheroid growth inside a cubic domain, Ω , of side length L , where L is chosen to be large enough so that agents do not reach the boundary of the domain during the simulation, but not so large as to incur significant computational overhead (Section 3.4.3). Biological cells are represented as discrete agents located at $\mathbf{x}_n(t) = (x_n(t), y_n(t), z_n(t))$ for $n = 1, 2, 3, \dots, N(t)$, where $N(t)$ is the total number of agents at time t .

Gillespie algorithm

The IBM describes key cellular-level behaviours; namely cell cycle progression and mitosis, cell motility, and cell death, as discrete events simulated using the Gillespie algorithm [46], where the time between events is sampled from the exponential distribution. Each agent has an allocated rate of cell cycle progression, dependent on its cell cycle status and the local nutrient concentration (Figure 2.2a). Agents in each phase of the cell cycle are coloured according to FUCCI, with G1 agents coloured red, eS agents coloured yellow, and S/G2/M agents coloured green.

We make the natural assumption that biological cells require access to sufficient nutrients to commit to entering the cell cycle. Therefore, the red-to-yellow transition rate, $R_r(c)$, depends on the local nutrient concentration, $c(\mathbf{x}, t)$ (Figure 2.2a). Once an agent has committed to entering the cell cycle, we assume the yellow-to-green transition takes place at a constant rate R_y , and the green-to-red transition, which involves mitosis, occurs at a constant rate R_g (Figure 2.2a).

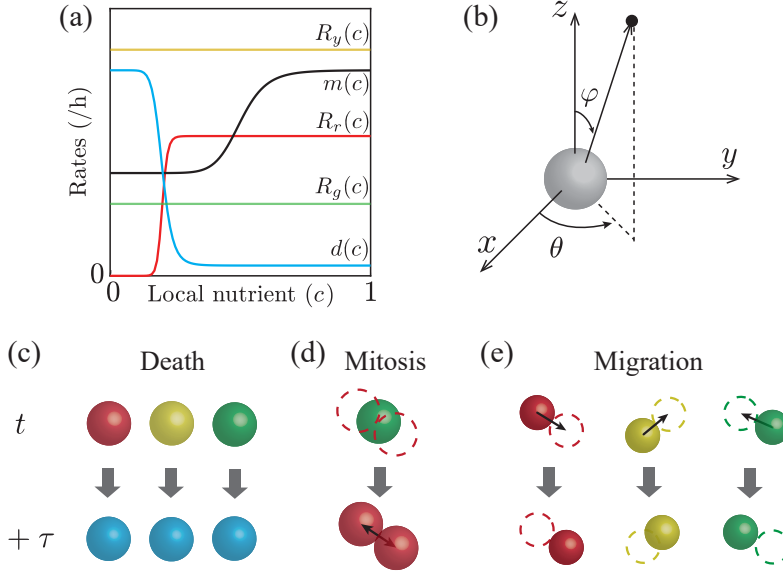


Figure 2.2: IBM schematic. (a) Nutrient-dependent rates (Equations (2.1)–(2.5)). (b) Random directions for migration and mitosis are obtained by sampling the polar angle θ , and the azimuthal angle φ separately [47]. (c)–(e) Schematics showing agent-level events; death, mitosis, and migration, across a time interval of duration τ . (c) Any living agent may die, removing it from the simulation. (d) An agent located at \mathbf{x}_n undergoes mitosis to produce two daughter agents in G1 phase and dispersed a distance of $\sigma/2$ from \mathbf{x}_n in opposite, randomly chosen directions. (e) Any living agent can migrate in a random direction with step length μ .

The rates of agent migration and death, $m(c)$ and $d(c)$, respectively, are assumed to depend on the local nutrient concentration. When an agent dies, it is removed from the simulation and we record the location at which the death event occurs (Figure 2.2c). When an agent moves or undergoes mitosis (Figure 2.2d-e), a random direction in which the agent will migrate, or its daughter agents will disperse, is chosen (Figure 2.2b). For an agent undergoing mitosis, the first daughter agent is placed a distance $\sigma/2$ along the randomly chosen direction, and the second daughter agent is placed at a distance $\sigma/2$ in the opposite direction, leaving the two daughter agents dispersed a distance of σ apart, where we set σ to be equal to a typical cell diameter [48] (Figure 2.2d, Table 2.1). When migrating, agents are displaced a distance μ along the randomly chosen direction (Figure 2.2e). Similarly to the dispersal, we simulate migration by taking the step length μ to be a typical cell diameter.

We specify the agent cycle progression rates,

$$R_r(c) = R_r \frac{c^{\eta_1}}{c_a^{\eta_1} + c^{\eta_1}}, \quad (2.1)$$

$$R_y(c) = R_y, \quad (2.2)$$

$$R_g(c) = R_g, \quad (2.3)$$

$$m(c) = (m_{\max} - m_{\min}) \frac{c^{\eta_2}}{c_m^{\eta_2} + c^{\eta_2}} + m_{\min}, \quad (2.4)$$

$$d(c) = (d_{\max} - d_{\min}) \left(1 - \frac{c^{\eta_3}}{c_d^{\eta_3} + c^{\eta_3}} \right) + d_{\min}, \quad (2.5)$$

where $c(\mathbf{x}_n, t) \in [0, 1]$ is the non-dimensional nutrient concentration at the location of the n th agent; $R_r > 0$ is the maximum red-to-yellow transition rate; $m_{\max} > m_{\min} \geq 0$ are the maximum and minimum migration rates, respectively; $d_{\max} > d_{\min} \geq 0$ are the maximum and minimum death rates, respectively; $\eta_1 > 0$, $\eta_2 > 0$, and $\eta_3 > 0$ are Hill function indices; and $c_a > 0$, $c_m > 0$, and $c_d > 0$ are the inflection points of $R_r(c)$, $m(c)$, and $d(c)$ respectively (Figure 2.2a).

Nutrient dynamics

We make the simplifying assumption that cell migration, death, and progression through the cell cycle are regulated by a single diffusible nutrient, such as oxygen [5, 10, 12]. The spatial and temporal distribution of nutrient concentration, $C(\mathbf{x}, t)$, is assumed to be governed by a reaction-diffusion equation

$$\frac{\partial C}{\partial t} = D \nabla^2 C - \kappa C v, \quad \text{in } \Omega, \quad (2.6)$$

with diffusivity $D > 0$ [$\mu\text{m}^2/\text{h}$], and consumption rate $\kappa > 0$ [$\mu\text{m}^3/(\text{h cells})$], and where $v(\mathbf{x}, t) \geq 0$ [$\text{cells}/\mu\text{m}^3$] is the cell density at position \mathbf{x} and time t . In the algorithm, we compute $v(\mathbf{x}_{i,j,k}, t)$ by considering the density of agents $N_{i,j,k}/h^3$ within the control volume surrounding the node located at (x_i, y_j, z_k) . We make the simple assumption that the nutrient diffusion is described by linear diffusion, and the source term explicitly describes the consumption of nutrient at a rate of κ [$\mu\text{m}^3/(\text{h cells})$]. On the boundary, $\partial\Omega$, we impose $C = C_b$, where C_b is some maximum far-field concentration.

Our experiments lead to spheroids of diameter 500–600 μm over a period of 10 days after spheroid formation (Figure 2.1) (14 days after seeding). Since these length and time scales are clear, we leave the independent variables \mathbf{x} and t in Equation (2.6) as dimensional quantities. In contrast,

spatial and temporal variations of $C(\mathbf{x}, t)$ are very difficult to measure during spheroid growth, so we non-dimensionalise the independent variable $c(\mathbf{x}, t) = C(\mathbf{x}, t)/C_b$, giving

$$\frac{\partial c}{\partial t} = D\nabla^2 c - \kappa cv, \quad \text{in } \Omega. \quad (2.7)$$

with $c = 1$ on $\partial\Omega$, and $c(\mathbf{x}, t) \in [0, 1]$.

Typically, the time scale of nutrient diffusion is much faster than the time scale of spheroid growth [10]. Consequently, we approximate Equation (2.7) by

$$0 = \nabla^2 c - \alpha cv, \quad \text{in } \Omega, \quad (2.8)$$

where $\alpha = \kappa/D > 0$ [$\mu\text{m}/\text{cells}$]. Therefore, we describe the spatial and temporal distribution of nutrients by solving Equation (2.8) repeatedly during the simulation. This quasi-steady approximation is computationally convenient, as we describe later. We solve Equation (2.8) with a finite volume method on a uniform structured mesh (Section 3.4) with node spacing h .

The IBM treats cells as lattice-free point particles, that we call agents. Interactions between agents are modelled implicitly by specifying rates of migration and cell cycle progression that depend upon the local nutrient concentration. As we will show later, this very simple framework replicates our experimental observations reasonably well, however we acknowledge there are other ways to treat agent-agent interactions, including lattice-based hard-core exclusion [48] and lattice-free methods for minimising [22] or avoiding agent overlap [41, 42]. Other options for modelling agent-agent interactions include direct simulation of agent adhesion or repulsion [49]. Instead, we use a simple framework to model agent migration. The random, fixed-step migration of the agents in the IBM allows for reasonably accurate modelling of our experimental spheroids. However, alternative approaches include explicitly modelling agent-agent interactions to bias agent migration [22], migration in response to the nutrient concentration or the nutrient concentration gradient, or by imposing a persistent correlated random walk so that agents are biased toward migration in the same direction as their last step [39]. While these mechanisms would encourage agents to continue on a consistent trajectory, we caution against this approach since implementing these mechanisms would also increase the number of parameters required for the model. Here, our modelling philosophy is to

work with the simplest possible biologically plausible model that can describe the key features of interest. Therefore, we deliberately avoid these additional mechanisms in our IBM framework.

In solving the nutrient concentration, one option for modelling the distribution of nutrient through the domain is to apply the boundary condition to the spheroid periphery. While this approach has been used successfully [24], we instead opt to allow the growth of the spheroid and the agent consumption of nutrient to influence the nutrient concentration in the surrounding medium. This approach is consistent with previous experimental works observing a nutrient gradient beyond the spheroid boundary [50–52], and has successfully been used to model tumour spheroid growth [23]. This approach will always have nutrient depletion near the boundaries of a finite domain, which can be increased or decreased as necessary (Section 3.4.3).

2.2.2 Simulation algorithm

We simulate spheroid growth by supposing the spheroid initially contains $N(0)$ agents distributed uniformly within a sphere of radius $r_o(0) > 0$ [μm]. While it is experimentally relevant to assume the population is spherically symmetric at $t = 0$, this assumption is not necessary, and we will discuss this point later. The proportion of agents chosen to be red, yellow, or green at $t = 0$ can be selected arbitrarily, but we choose these proportions so that the internal structure and composition of the *in silico* spheroids are consistent with our *in vitro* measurements. We achieve this by choosing the initial red, yellow, and green population, $N_r(0)$, $N_y(0)$, and $N_g(0)$, respectively, noting that $N(0) = N_r(0) + N_y(0) + N_g(0)$ (Section 3.8). The most appropriate time scale for individual cell-level behaviour is hours, however spheroid development takes place over 10 days, so we will use a mixture of time scales to describe different features of the experiments and simulations as appropriate. We simulate spheroid growth from $t = 0$ to $t = T$ h, updating the nutrient concentration at M equally-spaced points in time. This means that the nutrient concentration is updated at intervals of duration $t^* = T/M$ [h]. The accuracy of our algorithm increases by choosing larger M (smaller t^*), but larger M decreases the computational efficiency. We explore this tradeoff and find that setting $t^* = 1$ h is appropriate (Section 3.4.4). When Equation (2.8) is solved for $c(\mathbf{x}, t)$, the value of $c(\mathbf{x}_n, t)$ at each agent is calculated using linear interpolation. These local nutrient concentrations are held constant for each agent while

resolving all the various agent-level events (cycling and proliferation, migration, death) from time t to time $t + t^*$. After resolving the appropriate agent-level events, we update the agent density before updating the nutrient profile again. Pseudo-algorithms for the IBM are provided (Section 3.9), and code to reproduce key results is available on [GitHub](#).

2.2.3 IBM image processing

To estimate $r_o(t)$, $r_a(t)$, and $r_n(t)$, we apply methods described in [38, 53, 54] to the IBM output. Briefly, we import the agent locations from a particular cross section, and map these locations to an $(L + 1) \times (L + 1)$ pixel image, increase the size of the agents to 12 pixels in diameter, and use edge detection to identify and estimate $r_o(t)$, $r_a(t)$, and $r_n(t)$ (Section 3.2). This procedure adapts the image processing approach for the experimental images so that it is applicable to the synthetic results from the IBM.

2.3 Results and Discussion

We now compare and analyse images and measurements from a range of *in vitro* experiments and *in silico* simulations. All experiments use the WM793B melanoma cell line, which takes approximately four days to form spheroids after the initial seeding [26]. This means that $t = 0$ days corresponds to four days after seeding to give the experimental spheroids sufficient time to form. Snapshots from the IBM correspond to a single realisation, however time-series data from the IBM are reported by averaging appropriate measurements across 10 simulations of the IBM. While we take great care to analyze the simulation images and the experimental images using the same image processing algorithm, the format of the experimental images is different to the format of the images produced by the IBM, and we do not explicitly account for these differences.

2.3.1 Parameter values

Table 2.1 summarises the parameter values used in this study. While some parameters are based on separate, independent two-dimensional experimental measurements (Section 3.5 – 3.6) or measurements directly from the spheroids where possible (Section 3.7), other parameters are chosen based on a series of numerical screening tests (Section 3.4). We will return to discuss other options for parameter choices later.

Table 2.1: IBM parameter values.

Parameter Name	Symbol	Value	Source
<i>Numerical Parameters</i>			
Initial number of agents	$N(0)$	30 000	Experimental measurement (Section 3.7)
Initial number of red agents	$N_r(0)$	20,911	Assumption (Section 3.8)
Initial number of yellow agents	$N_y(0)$	995	Assumption (Section 3.8)
Initial number of green agents	$N_g(0)$	8,094	Assumption (Section 3.8)
Domain length	L	4000 μm	Numerical experiments (Section 3.4.3)
Initial spheroid radius	$r_o(0)$	245 μm	Experimental measurement
Dispersal distance	σ	12 μm	Assumption (Section 3.5)
Migration distance	μ	12 μm	Assumption (Section 3.5)
Simulation termination time	T	240 h	Experimental measurement
<i>Per Capita Agent Rates</i>			
Maximum G1-eS transition rate	R_r	0.047 /h	Experimental measurement (Section 3.6)
Constant eS-S/G2/M transition rate	R_y	0.50 /h	Experimental measurement (Section 3.6)
Constant S/G2/M-G1 transition rate (mitosis)	R_g	0.062 /h	Experimental measurement (Section 3.6)
Maximum death rate	d_{\max}	2 /h	Assumption
Minimum death rate	d_{\min}	0.0005 /h	Assumption
Maximum migration rate	m_{\max}	0.12 /h	Assumption
Minimum migration rate	m_{\min}	0.06 /h	Assumption
Hill function index for arrest	η_1	5	Assumption
Hill function index for migration	η_2	5	Assumption
Hill function index for death	η_3	15	Assumption
<i>Nutrient Parameters</i>			
Number of nodes	I^3	201^3	Assumption (Section 3.4.4)
Steady-state solution interval	t^*	1 h	Assumption (Section 3.4.4)
Consumption-diffusion ratio	α	0.15 $\mu\text{m}/\text{cells}$	Assumption
Critical arrest concentration	c_a	0.4	Assumption
Critical migration concentration	c_m	0.5	Assumption
Critical death concentration	c_d	0.1	Assumption

2.3.2 Qualitative comparison of experiments and simulations

We now qualitatively compare images of *in vitro* (Figure 2.3a,c,e) and *in silico* (Figure 2.3b,d,f) spheroids by imaging various cross sections at different locations, including the equator (Figure 2.3a-b), the lower cross section (Figure 2.3c-d), and the upper cross section (Figure 2.3e-f). We use the definitions in Section 3.1 (Confocal imaging) to identify the lower and upper cross sections in the analysis of both the experimental images and the simulation images. While previous studies have often compared model predictions with experimental observations at a single cross section [24, 26], we aim to provide more comprehensive information about the internal structure of the spheroid by making comparisons at multiple locations.

At the beginning of the experiment, in all cross sections (*in vitro* and *in silico*) we see the population is relatively uniform, with an even distribution of colours, suggesting the entire spheroid is composed of freely-cycling cells. At $t = 2$ and $t = 4$ days, however, we begin to see the development of heterogeneity within the growing *in vitro* and *in silico* populations, with those cells and agents at the centre of the growing spheroid predominantly red, indicating G1-arrest. By $t = 4$ days we see the value of comparing different cross sections, since the G1-arrest is clear in the centre of the equatorial cross section, but there is no obvious heterogeneity present across either the upper or lower cross section at that time. Similarly, by $t = 6$ days we see the formation of a necrotic core in the equatorial cross section, but this is not present at either cross section. By $t = 8$ and $t = 10$ days the spheroid has developed into a relatively complicated heterogeneous structure where the outer spherical shell contains freely cycling cells, the intermediate spherical shell contains living G1-arrested cells, and the internal region does not contain any fluorescent cells.

Overall, the qualitative match between the IBM and the experiment confirms that the IBM captures both the macroscopic growth of the entire spheroid, as well as the emergent spatial and temporal heterogeneity. We now build on this preliminary qualitative information by extracting quantitative measurements of the spheroid growth and exploring the performance of the IBM.

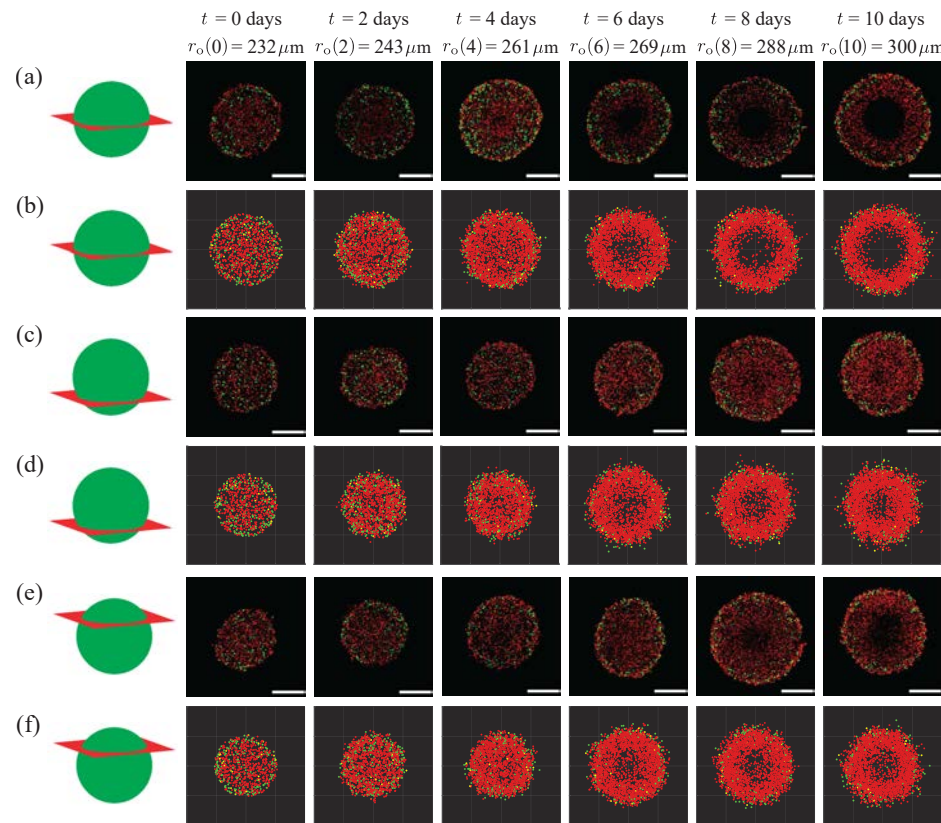


Figure 2.3: Comparison of *in vitro* and *in silico* 4D spheroids. Experimental results (a,c,e) are compared with simulation results (b,d,f) by examining 2D slices at the equator, lower and upper cross section, respectively. Agent colour (red, yellow, green) corresponds to FUCCI labelling (G1, eS, S/G2/M). Schematics in the left-most column indicate the location of the 2D cross section. The images are taken at (a)–(b) the equator, (c)–(d) the lower cross section, and (e)–(f) the upper cross section. Experimental spheroid radii at the equator are labelled at each time point, and scale bars represent $200 \mu\text{m}$.

2.3.3 Spheroid structure and nutrient profiles

Given the ability of the IBM to capture key spatial and temporal patterns of spheroid growth, cell cycle arrest, and cell death throughout the spheroid, we now demonstrate how to take these preliminary simulations and extract detailed quantitative data that would be difficult to obtain experimentally. Figure 2.4a shows a typical IBM simulation during the interval where we observe the development of internal structure. For clarity, we plot the locations of all living agents as in Figure 2.3 together with the locations at which agents die, which is difficult to estimate experimentally, but is straightforward with the IBM. Each spheroid in Figure 2.4a is shown with an octant removed to highlight the development of the internal structure, and for further clarity we show equatorial cross sections in Figure 2.4b.

To quantify the internal spheroid structure we simulate 10 identically prepared realisations of the IBM and extract averaged quantitative data that are summarised in Figure 2.4c (Section 3.10). These data include plotting the nondimensional nutrient concentration, $c(\mathbf{x}, t)$, and various normalised agent densities, $\varrho(p(t), t)$, as a function of distance from the spheroid periphery, $p(t) = r_o(t) - r$, where r is the distance from the spheroid centre. Hence, $p(t) = 0$ at the spheroid periphery, and $p(t) = r_o(t)$ at the spheroid centre. This representation of internal spheroid structure is made by assuming that the growing population remains spherically symmetric, which is a reasonable assumption since our initial condition and spheroid growth is spherically symmetric (Figure 2.4a). Each density profile is normalised relative to the maximum value of all agent densities across all time points, so that we can compare how the density of the various sub-populations of agents and nutrient are distributed (Section 3.10). Using the IBM we are able to describe the spatial and temporal densities of living agents in various phases of the cell cycle (G1, eS and S/G2/M) as well as G1-arrested agents. We plot each density profile as a function of the distance from the periphery as this allows us to compare various profiles as the size of the spheroid increases [25, 55].

Averaged relative agent density profiles from the IBM provide quantitative information that cannot be easily obtained from experimental observations. Initially we see the relatively evenly distributed G1, eS and S/G2/M populations become rapidly dominated by agents in G1 phase, which then form an obvious inner-most arrested region by about $t = 2$ days. During the interval $3 < t < 6$ days, we observe rapid growth in the arrested popu-

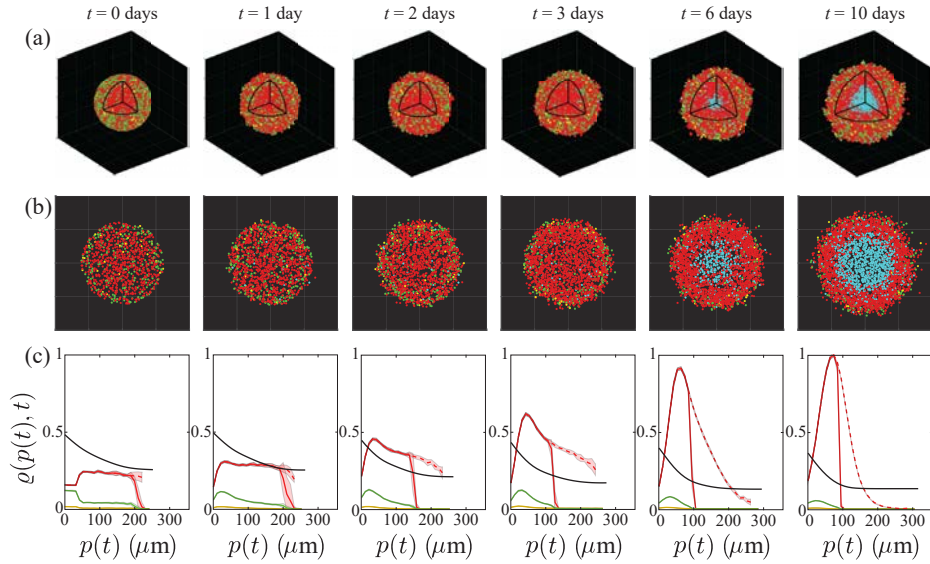


Figure 2.4: Typical IBM simulation, showing: (a) visualisations of *in silico* spheroids including dead agents (cyan) and (b) cross sections through the spheroid equator with dead agents. (c) Relative concentrations $\varrho(p, t)$ of nutrient (black) and cycling red, yellow, and green agents (coloured appropriately), based on distance from the periphery $p(t) = r_o(t) - r$, averaged over 10 identically-prepared simulations. The dashed red line shows the relative density of arrested red agents, also averaged over 10 simulations with identical initial conditions. For nutrient, $\varrho(p, t) = c$. For agents, $\varrho(p, t)$ is the relative agent density (Section 3.10). Shaded areas represent plus or minus one standard deviation about the mean, and are non-zero as a consequence of stochasticity in the model, even though the 10 simulations start with identical populations and radii.

lation. During the later interval, $6 < t < 10$ days, we see the formation of a clear necrotic core. These results indicate the spatial and temporal role of stochasticity, with the variability most evident in the G1 and arrested G1 populations at early times. Plotting the relative agent densities in this way provides a simple approach to interpret the spatial and temporal organisation of cell cycle status within the growing spheroid, and visualising the agent densities together with the nondimensional nutrient concentration is particularly useful when this kind of information cannot be easily obtained experimentally. In particular, it is technically challenging to measure absolute concentrations of nutrient profiles during these experiments [17, 56, 57] and so we now focus on visualising the nutrient concentration profile that drives this heterogeneity.

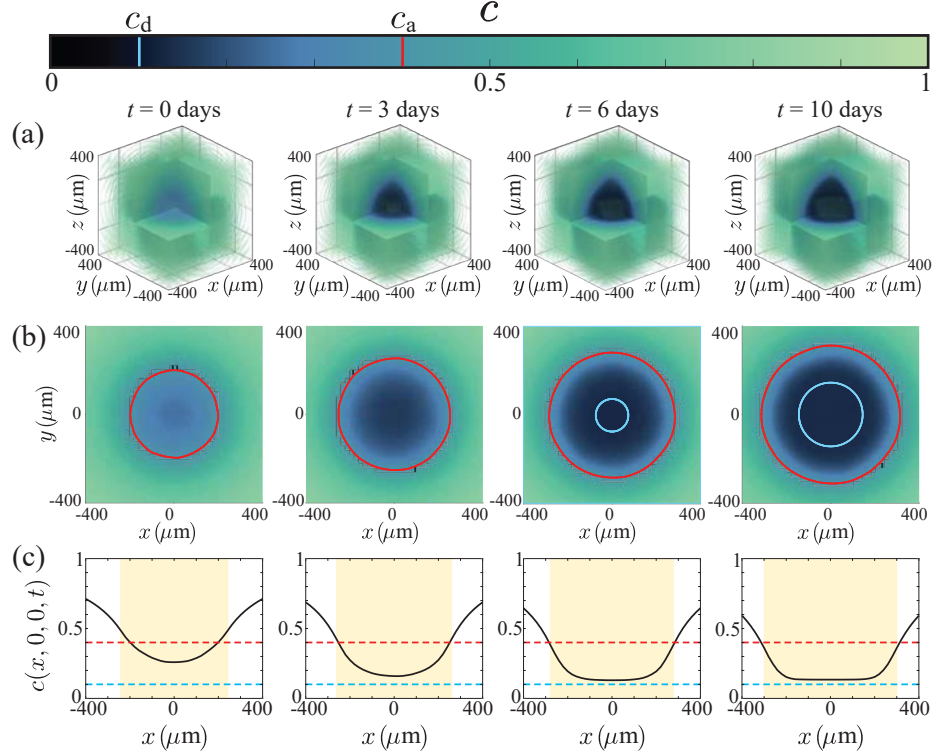


Figure 2.5: Nutrient concentration profiles (a) in three spatial dimensions, (b) at the equator $z = 0$, with the arrest critical level c_a shown in red, and the size of the necrotic region in white. (c) Nutrient profiles along the midline $y = z = 0$, where the shaded region represents the size of the spheroid, and the red and cyan lines are the critical levels for arrest and death, c_a and c_d respectively. The colourbar corresponds to the profiles in (a)–(b), and denotes the values c_a (red) and c_d (cyan).

Results in Figure 2.5 show spatial and temporal patterns in the nutrient profile, $c(\mathbf{x}, t)$, for a typical IBM simulation from Figure 2.4. Figure 2.5a shows the three-dimensional evolution of $c(\mathbf{x}, t)$, with the colourbar highlighting the death and arrest thresholds, c_d and c_a , respectively. These three-dimensional plots show the depletion of nutrient over time in the central region of the spheroid, leading to strong spatial gradients of nutrient concentration near the edge of the growing spheroid. Profiles in Figure 2.5b show the nutrient profile at the equatorial plane with the $c(x, y, 0) = c_a$ contour (red) and the approximate size of the necrotic core (cyan) superimposed. Simplified one-dimensional profiles of $c(\mathbf{x}, t)$, along $\mathbf{x} = (x, 0, 0)$, are shown in Figure 2.5c, where the diameter of the growing spheroid ($-r_o(t) < x < r_o(t)$) is shaded in yellow. Again, these simplified

cross sections illustrate how nutrient consumption leads to the formation of spatial nutrient gradients near the outer radius of the growing spheroid. Overall, a key strength of the IBM is the ability to extract agent-level information (Figure 2.4) as well as information about the nutrient distribution (Figure 2.5), whereas experimental studies typically report cell-level data without explicitly showing nutrient-level information [5, 36].

While it is very difficult to measure the spatial and temporal distribution of diffusible nutrient experimentally in the growing spheroid, it is possible to indirectly examine our assumption that spatial and temporal differences in cell cycle status are partly driven by the availability of oxygen. Figure 2.6 shows a series of spheroids stained with pimonidazole and pimonidazole-detecting antibodies, which indicate hypoxia [58]. In this series of images, we see evidence of hypoxia staining in the central region of the spheroid at $t = 0$, with persistent hypoxia staining adjacent to the necrotic core at later times. These results support our hypothesis that spatial and temporal differences in nutrient availability correspond with spatial and temporal differences in cell cycle status, and in this case the pimonidazole staining suggests that oxygen availability plays a role in the development of heterogeneity within the growing population. While this observation is consistent with our IBM, it does not rule out the possibility of multiple diffusible signals acting in unison, and we will discuss this possibility later.

2.3.4 Role of variability

Experimental images (Figures 2.1, 2.3 and 2.6) suggest that spheroid development is variable, as we see spheroids of different diameters at the same time points. One of the limitations of relying on experimentation alone is that it can be difficult to quantify the importance of different sources of variability, whereas this can be assessed very simply with the IBM. For example, we can simulate multiple spheroids that start from precisely the same initial condition to quantify the variability that arises due to the stochastic growth process, or we can deliberately introduce variability into the initial composition of the spheroid to explore how this variability evolves during spheroid growth for a suite of simulated spheroids.

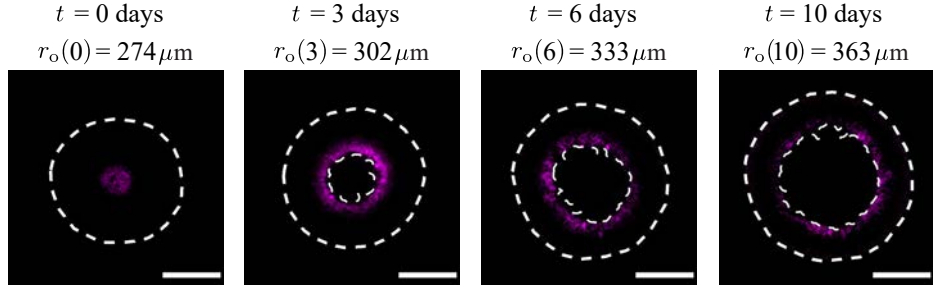


Figure 2.6: Spheroids stained for hypoxia at 0, 3, 6, and 10 days after spheroid formation, imaged at the spheroid equator. Hypoxia-positive staining fluoresces magenta, and white dashed lines denote $r_o(t)$ and $r_n(t)$, detected with image processing, to contextualise the regions of hypoxia. For clear visualisation, we label the outer radii of the spheroid with the corresponding days. Image intensity was adjusted for visual purposes, and scale bar corresponds to 200 μm .

Simulation data in Figure 2.7a show the temporal evolution of various agent subpopulations, including the total number of living agents, dead agents, G1, eS, S/G2/M, and G1-arrested agents. Each profile shows the mean number of agents obtained by simulating 10 identically initialised spheroids with $r_o(0) = 245 \mu\text{m}$, which matches the average spheroid diameter at $t = 0$ days in the suite of *in vitro* experiments. The variability in these profiles is quantified by calculating the sample mean and sample standard deviation and shading the region corresponding to the sample mean plus or minus one sample standard deviation, and we see that, at this scale, the variability is barely noticeable. In contrast, results in Figure 2.7b show equivalent data from a suite of simulations where the initial density of agents in the spheroid is held constant, but the initial radius of the 10 simulated spheroids is deliberately varied to mimic the observed variability in our experiments. The initial radius in each simulation corresponds to one of 10 particular experimental measurements (Figure 2.7), with a sample mean of $\bar{r}_o(0) = 245 \mu\text{m}$. Comparing results in Figure 2.7a-b shows that the average population profiles are very similar, but the variability is strikingly different. This simple exercise shows that quantifying the variability in spheroid size at the beginning of the experiment is the key to understanding and predicting the variability in spheroid composition and size at the end of the experiment. We also see that 10 simulations is sufficient to observe the difference in variability between both test cases, where the spheroids start from identical initialisations or with induced variability.

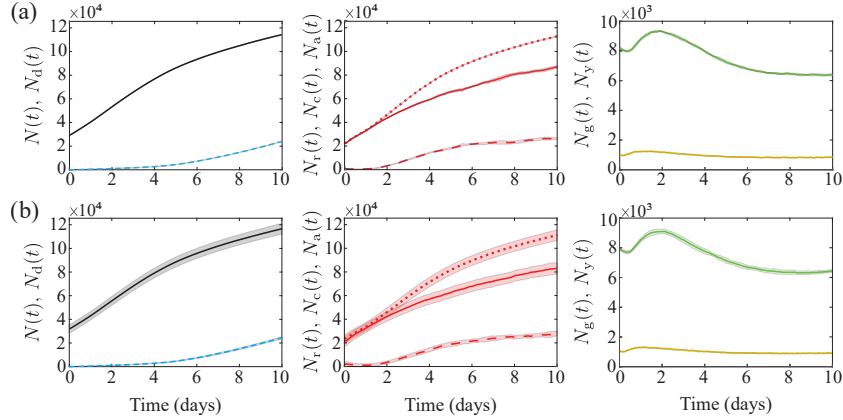


Figure 2.7: Modelling results for the population growth of different spheroid populations, averaged over 10 simulations with (a) identical initial conditions for each realisation and (b) introduced experimental variability in initial spheroid radius and population, with the agent density held constant and initial radius $r_o(t) \in [232.75, 235.47, 238.97, 242.19, 244.89, 247.76, 247.93, 251.23, 251.48, 260.13] \mu\text{m}$. In each row, left: living (black) and dead (cyan dashed) populations, $N(t)$ and $N_d(t)$, respectively, centre: arrested red (dashed), cycling red (solid), and total red (dotted) populations, $N_a(t)$, $N_c(t)$, and $N_r(t)$, respectively, and right: yellow and green populations, $N_y(t)$ and $N_g(t)$, respectively. Shaded areas represent plus or minus one standard deviation. Initial subpopulations in each simulation in both (a) and (b) are variable, as initial cell cycle status is assigned randomly (Section 3.8), and so the initial subpopulations in (b) also naturally vary with the overall initial population, $N(0)$.

These simulation results are also consistent with our previous observations. For example, the *in vitro* spheroids in Figure 2.3 have $r_o(0) = 232 \mu\text{m}$ and we see that it takes until $t = 6$ days for a clear necrotic core to form in the equatorial cross section. In contrast, the spheroid in Figure 2.6 is larger with $r_o(0) = 274 \mu\text{m}$ and we see a clear necrotic core at $t = 3$ days. This highlights the importance of taking great care with measurements at the beginning of the experiment [26].

2.3.5 Quantitatively matching experimental and mathematical spheroids

Results in Figure 2.8 compare the temporal evolution of $r_o(t)$, $r_a(t)$, and $r_n(t)$, from our suite of experiments and simulations. The data in Figure 2.8 show the value in working with a stochastic model since the experimental

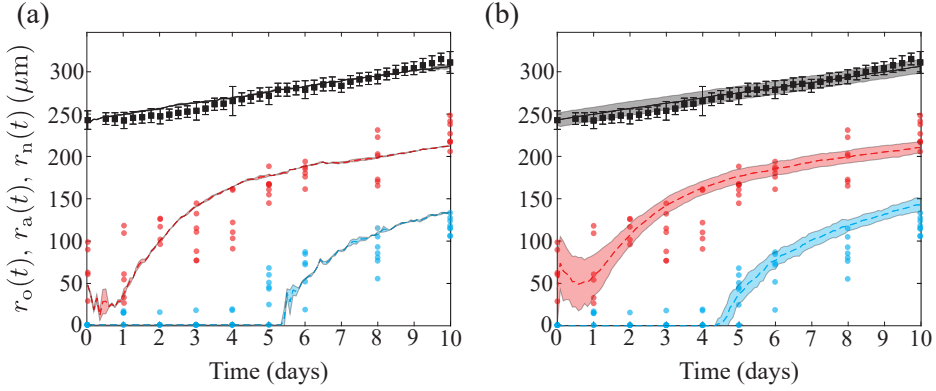


Figure 2.8: Comparison of computational estimates of $r_o(t)$ (black), $r_a(t)$ (red), and $r_n(t)$ (cyan) with experimental data. The experimental data (dots) are compared with (a) simulations with each run starting with an identical parameter set and (b) simulations with variations of the initial spheroid radius and population, with each initial radius selected from experimentally measured radii at $t = 0$ days and agent density kept constant. Computational results are the average of 10 simulations, and error regions represent plus or minus one standard deviation. The initial subpopulations vary in both (a) and (b), due to randomly assigning cell cycle status (Section 3.8). In (b), we also naturally see higher variations in each subpopulation initially, due to explicitly including initial population variability, which in turn induces variability in $r_a(0)$.

measurements are quite variable, with estimates of $r_a(t)$ and $r_n(t)$ more variable than estimates of $r_o(t)$. This difference in variability is because we measure $r_o(t)$ automatically with an IncuCyte S3 every 6 hours. In contrast, measurements of $r_a(t)$ and $r_n(t)$ require manual harvesting, fixing, and imaging, and accordingly we report these measurements daily.

Similarly to Section 2.3.4, we compare experimental results of average data in simulations with and without induced variability in the initial condition. The experiment-IBM comparison in Figure 2.8a corresponds to the case where we simulate 10 identically-prepared realisations of the IBM, where each simulated spheroid has the same initial radius $r_o(0) = 245 \mu\text{m}$, and we see that the average simulation results capture the average trends in the experimental measurements well, but the IBM simulations do not capture observed variability in the evolution of $r_a(t)$ or $r_n(t)$. In contrast, the experiment-IBM comparison in Figure 2.8b, where we deliberately mimic the experimental variability at $t = 0$, captures both the average experimental trends and variability in the experimental data quite well. Again, the difference between Figure 2.8a-b suggests that incorporating the initial

variability in the experimental data is critical if we wish to capture the observed variability in the experiments.

Interestingly, our experimental data in Figure 2.8 suggest that we have an approximately linear increase in $r_o(t)$ over time, whereas the development of the internal structure is more complicated. The initial arrested radius decreases for the first day before growing rapidly, and we do not see the formation of a necrotic core until approximately $t = 4$ days. While our IBM-experimental comparison in Figure 2.8 suggests that the IBM can quantitatively capture experimental trends, we have obtained this match with a careful choice of parameters without undertaking a more rigorous parameter estimation exercise [59]. The sensitivity of the IBM predictions to the parameter values is briefly explored in the Chapter 3.11.

2.4 Conclusions and Future Work

We developed an IBM that simulates 4D tumour spheroids with FUCCI. IBM simulations reveal that we can successfully reproduce qualitative and quantitative patterns of spatial and temporal differences in cell cycle status that we observe in *in vitro* experiments. This heterogeneity is driven by spatial and temporal variations in nutrient availability, which we model using a reaction-diffusion equation coupled to the IBM.

An important advantage of the IBM is our ability to extract and describe measurements that are difficult to obtain *in vitro*. In particular, we show how to visualise both the growing populations within the spheroid together with the spatial patterns of nutrient concentration over time within the growing spheroid. Furthermore, the IBM makes it very simple to explore how various features contribute to the overall variability in spheroid development, and we find that relatively small variations in the initial size of the spheroid lead to relatively pronounced differences in spheroid size and composition at later times [26]. We conclude our investigation by showing that we can quantitatively match the spatial and temporal development of a series of *in vitro* 4D spheroids using the WM793B human primary melanoma cell line with a careful choice of parameters. We anticipate that tumour spheroids formed with different cell lines will be able to be simulated with our IBM, but will require different parameter values.

Overall, our modelling philosophy is always to work with the simplest possible mechanisms required to capture our experimental observations. Naturally, this means that there are many ways that the IBM can be ex-

tended. For example, here we make the simple assumption that spheroid growth is regulated by a single diffusible nutrient, which seems appropriate for our data. If, however, experiments show that it is important to consider multiple nutrients in unison, our IBM framework can be extended to deal with this. Similarly, we focus on symmetric spheroid growth to be consistent with our experiments, but it is straightforward to relax this assumption by specifying a different initial arrangement of agents, or by allowing asymmetric nutrient delivery by, for example, a blood vessel, as we explore in Chapter 3.12. Another point that could be revisited is that we implement the simplest possible cell migration mechanism where the direction of motion is random. While this assumption appears reasonable for our data, it is possible to bias the migration in response to either the nutrient concentration, the gradient of the nutrient concentration, or the density of agents by explicitly describing agent-to-agent interactions [22]. Each of these potential extensions could be incorporated into our IBM framework with the aim of potentially increasing the biological fidelity of the model. However, here we caution against this approach since these mechanisms also increase the number of parameters required for simulation. To minimise issues with parameter identifiability, we prefer to work with a minimal model [59]. If, however, future experimental measurements indicate that our minimal assumptions need to be revised, our IBM framework is sufficiently flexible to incorporate such extensions, if warranted. Another option for future refinement is to conduct a more thorough parameter estimation exercise. Here we carefully chose parameters that appear to match our data, but future analysis could include a more rigorous assessment of parameter estimation, and we leave this for future consideration.

Chapter 3

Supporting information for a stochastic mathematical model of 4D tumour spheroids

3.1 Experimental methods

Spheroid growth and staining: Human melanoma cells from the WM793B cell line were genotypically characterised [60–62], grown as described in [2], and authenticated by short tandem repeat fingerprinting (QIMR Berghofer Medical Research Institute, Herston, Australia). The WM793B cells were transduced with FUCCI constructs [5]. Spheroids were seeded, grown on hard agarose, and stained as in [2], with 1% penicillin-streptomycin (ThermoFisher, Massachusetts, USA). Three 96-well plates of spheroids, seeded with a density of 10,000 cells per well, were grown and harvested over 14 days. One 96-well plate was placed in an IncuCyte S3 (Sartorius, Göttingen, Germany) and imaged at 6 hour intervals over 14 days. Harvested spheroids were stained with either DRAQ7 (ThermoFisher, Massachusetts, USA) for necrosis or pimonidazole for hypoxia, fixed in 4% paraformaldehyde solution, and stained with DAPI as per [63].

To reveal the hypoxic region, spheroids stained with pimonidazole were permeabilised with 0.5% triton X-100 in phosphate buffered solution (PBS) for one hour, then blocked in antibody dilution buffer (Abdil) [64] for 24 hours. Spheroids were stained with a 1:50 anti-pimonidazole mouse IgG1

monoclonal antibody (Hypoxyprobe-1 MAb1) in Abdil for 48 hours, before washing in PBS with 0.1% tween-20 for six hours. These spheroids were then placed in a 1:100 solution of Alexa Fluor 647 in Abdil for 48 hours. Following this, the spheroids were washed for six hours in PBS.

Confocal imaging: Harvested spheroids were mounted in 2% low melting agarose in PBS solution and cleared in clearing reagent 2 with matching refractive index [63], on #1.5 glass bottom plates. For collecting 2D cross sections, images were taken at the equator and upper and lower cross sections (Figure 2.1b), which we define as the Z coordinate halfway between the equator and the top or bottom of the spheroid. If the necrotic core exists, the upper and lower cross sections are at the top or bottom of the necrotic core, respectively. 3D spheroid images were collected by imaging over the entire Z range of the spheroid.

Computational image analysis: The image processing algorithm [54] was used to estimate $r_o(t)$, $r_a(t)$, and $r_n(t)$.

3.2 Image processing

The image processing algorithm for experimental images uses the algorithm presented and described in [54]. Here, we describe the procedure used to prepare the synthetic data from the IBM for estimates of $r_o(t)$ and $r_n(t)$. We perform the image analysis on synthetic data in MATLAB as follows:

1. An image of $(L + 1) \times (L + 1)$ pixels is created, so that each pixel is one micrometre in length, and all agents within $18 \mu\text{m}$ of $z = 0$ have their x and y coordinates recorded,
2. Living agents from the synthetic dataset are rounded to their nearest integer location with `round` and placed at the corresponding pixel in the image with `sub2ind`,
3. Each agent is increased in size to a diameter of σ pixels,
4. Components of the binarised image with a connected area less than a threshold value A are removed by area opening with `bwareaopen`, where A is sufficiently large so that only the contiguous spheroid remains,

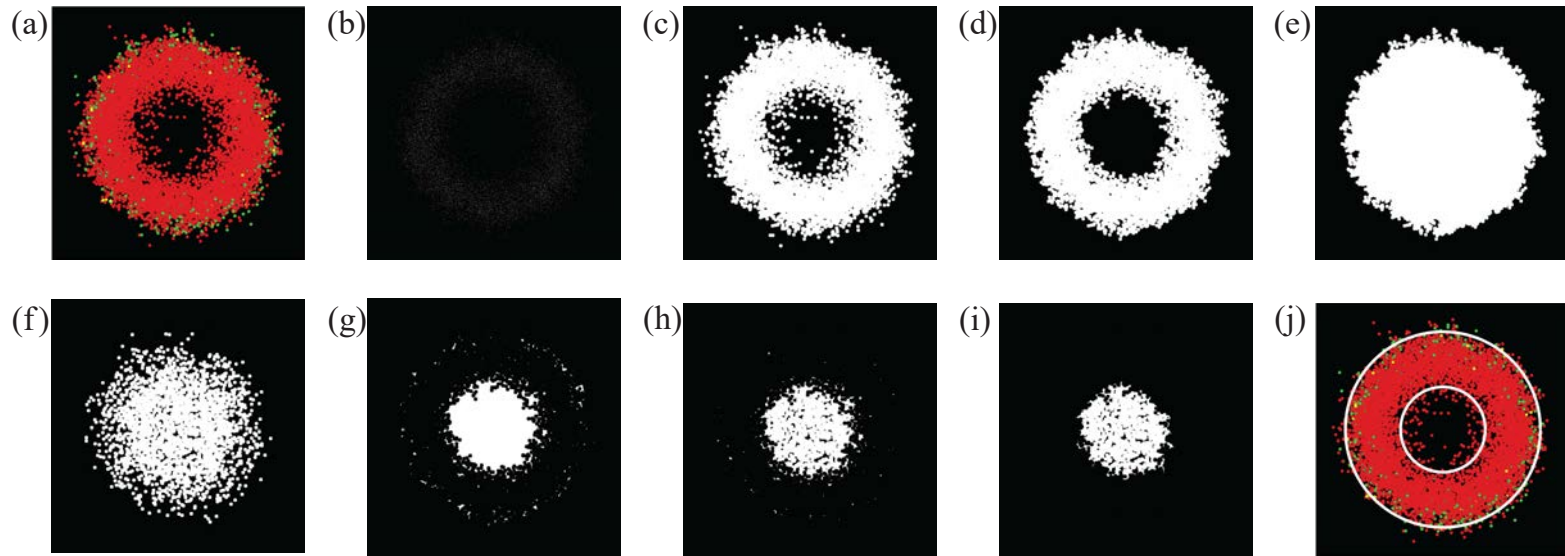


Figure 3.1: Example of applying the radius estimate image processing algorithm to a synthetic dataset. (a) A 2D slice at the equator of the spheroid, (b) the agents are mapped into a single pixel each at their equivalent positions on a binary, $(L+1) \times (L+1)$ image. The agent size is then increased, as shown in (c), to better represent their equivalent physical representation, before area opening (d) and filling the remaining space (e). The radius of a circle with equivalent area to the filled space is calculated, and used as the estimate for the outer radius, $r_o(t)$. (f) The mask of dead agents is created, along with (g) a mask of the empty space inside the spheroid in (d). (h) The intersection between the dead agent mask and the empty space, and (i) the clearing of (h) to only the largest continuous area. If this region is large enough, the necrotic region is taken to be the largest area in (g), and its radius, $r_n(t)$, is the radius of a circle with equivalent area. (j) The estimates for $r_o(t)$ and $r_n(t)$ are shown plotted over the original spheroid slice.

5. Remaining holes are filled (`imfill`) and remaining peripheral segments disconnected from the main body are removed (`imclearborder`),
6. The area enclosed by the boundary is calculated with `regionprops`, and $r_o(t)$ is estimated by assuming the region is circular, and calculating the radius of a circle with an equivalent area,
7. A mask of dead agents is created according to steps 1–3,
8. The intersection between the dead agent mask and the space left unfilled by the living agents before performing step 5 is found,
9. If the radius of a circle with equivalent area to this intersection is smaller than $2\Delta_c$ (too small to be meaningful in the context of a necrotic core), set the necrotic radius, $r_n(t) = 0$,
10. Otherwise, $r_n(t)$ is set as the radius of a circle with equivalent area to the filled space of the dead agent mask.

An example of this procedure is visualised in Figure 3.1.

Similarly to the estimates of $r_o(t)$ and $r_n(t)$, we estimate $r_a(t)$ with MATLAB, and the procedure is designed to mimic the procedure used for estimating the arrested radius in experimental images, outlined in [54]. Visualisation of this process is given in Figure 3.2. We prepare the synthetic data as follows:

1. Each green agent from the synthetic dataset at time t is converted from its 3D Cartesian coordinate, \mathbf{x}_n , to its radial coordinate, r_n , with the transformation

$$r_n = \|\mathbf{x}_n - \bar{\mathbf{x}}(t)\|, \quad n = 1, \dots, N_g(t), \quad (3.1)$$

where $N_g(t)$ is the number of green agents at time t and $\bar{\mathbf{x}}(t)$ is the mean location of all agents in the spheroid at time t (Figure 3.2a), and $\|\cdot\|$ is the Euclidean length,

2. The green agents are organised into a distribution of radial position, $G(r_l)$, where r_l are the centres of the bins with binwidth $w = 20 \mu\text{m}$, so that $l = 0, \dots, \text{round}(r_o(t)/w)$. We set $l_{\max} = \text{round}(r_o(t)/w)$ as this maximum index. The binwidth $w = 20 \mu\text{m}$ is chosen to be sufficiently small to best identify spatial information about the radial distribution of green agents, but also large enough to avoid fluctuations in the distribution [65],
3. The agent density, $g(r_l)$, is calculated by dividing the agent count distribution, $G(r_l)$, by the radial volume,

$$g(r_l) = \frac{3G(r_l)}{4\pi \left(\left(r_l + \frac{w}{2} \right)^3 - \left(r_l - \frac{w}{2} \right)^3 \right)}, \quad l = 0, \dots, l_{\max}, \quad (3.2)$$

4. The agent density is then normalised, such that

$$\hat{g}(r_l) = \frac{g(r_l)}{\max(g(r_l))}, \quad l = 0, \dots, l_{\max}, \quad (3.3)$$

where the $\max(g(r_l))$ is the maximum of the green agent density at time t ,

5. A Gompertz function,

$$\hat{g}_G(r) = \gamma_1 \exp(-\exp(\gamma_2(\gamma_3 - r))), \quad (3.4)$$

is fit to the normalised agent density distribution, $\hat{g}(r_l)$, on the domain $r \in [0, \arg \max(\hat{g}(r_l))]$ using the method of least squares to create a smoothed normalised green agent density as a function of radial position, $\hat{g}_G(r)$ (Figure 3.2b). The values $\gamma_1, \gamma_2, \gamma_3$ are the parameters fit by the method of least squares. This choice of domain, from $r = 0$ to $r = \arg \max(\hat{g}(r_l))$, is used because it generates a more accurate fit of $\hat{g}_G(r)$ to $\hat{g}(r_l)$ in the region of interest, due to the shapes of the Gompertz function and normalised agent density function, $\hat{g}(r_l)$,

6. Adapting the method in [54], if $\hat{g}_G(0) > g_a$, then $r_a(t) = 0$. Otherwise, $r_a(t)$ is defined such that $\hat{g}_G(r_a(t)) = g_a$. We use the tunable threshold parameter $g_a = 0.2$, so that the arrested region is considered to be the boundary where the smoothed relative green agent density function surpasses 0.2.

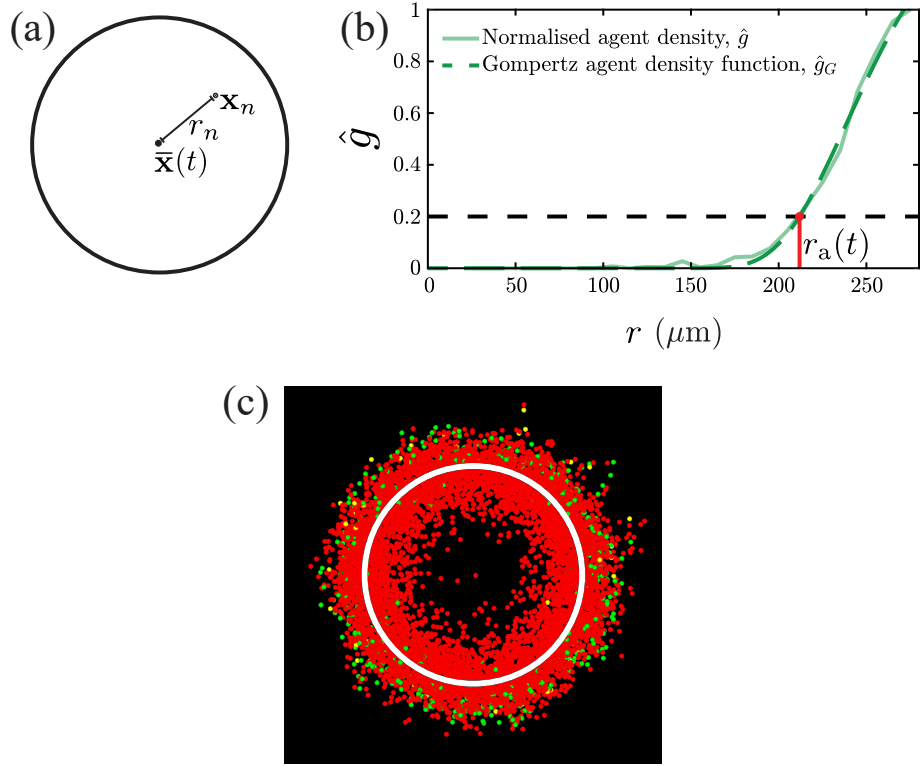


Figure 3.2: Example of how the arrested radius is estimated with synthetic data. (a) The 3D Cartesian position of a green agent, \mathbf{x}_n , is converted into a radial coordinate, r_n , by calculating its Euclidean distance from the mean position of all agents in the spheroid, $\bar{\mathbf{x}}(t)$. (b) An example of the normalised green agent density distribution, $\hat{g}(r_l)$, and the Gompertz function of smoothed agent density, $\hat{g}_G(r)$, for a spheroid at late time. The arrested radius, $r_a(t)$ is calculated as the value of r for which $\hat{g}_G(r) = g_a$, where $g_a = 0.2$. (c) An example spheroid slice, with an estimate of $r_a(t)$ shown, calculated using the above method.

3.3 Benchmarking the 3D numerical partial differential equation solution

To ensure our spatial discretisation of the 3D partial differential equation (PDE) model of the nutrient profile is accurate, we first solved a number of simpler test cases with exact solutions. To this end, we consider an infinite domain 3D diffusion-decay problem where some mass of diffusing substance, S , is placed at the origin at $t = 0$ [66]. The governing equation is

$$\frac{\partial c}{\partial t} = D\nabla^2 c - \kappa c, \quad (3.5)$$

with diffusivity $D > 0$ and decay rate κ . The exact solution is,

$$c(r, t) = \frac{S}{(2\sqrt{\pi Dt})^3} \exp\left(-\frac{r^2}{4Dt} - \kappa t\right), \quad (3.6)$$

where $r = \sqrt{x^2 + y^2 + z^2}$ [66].

To test the accuracy of our numerical method, we consider this problem on a truncated finite domain. In this case we consider a cube of side length $L = 20$, with the origin at the centre of the cube. We discretise the truncated domain using a uniform mesh with node spacing $h = 0.2$ so that our mesh contains 101^3 nodes. In our numerical simulations, we impose homogeneous Dirichlet boundary conditions along all boundaries. The numerical solution is obtained by discretising the flux and source terms in Equation (3.5) on the finite volume mesh in exactly the same way as for the nutrient model in the main document. This leads to a system of coupled ordinary differential equations that we solve in time using MATLAB's `ode45` solver [67]. Results in Figure 3.3 compare exact and numerical solutions along the $y = z = 0$ midline for $x \in [-5, 5]$. In Figure 3.3a we consider a conservative problem where $\kappa = 0$, and in Figure 3.3b we consider a diffusion-decay problem with $\kappa > 0$. In all cases the numerical solution matches the exact solution well, giving us confidence in our spatial discretisation method.

We set the total amount of mass diffusing through the domain at $S = 100$ and use diffusivity $D = 1$, and consider two decay parameters, $\kappa = 0$ (diffusion without a source term) and $\kappa = 0.3$. In Figure 3.3, we compare exact and numerical solutions at $t = 1$, $t = 1.5$, and $t = 2$. Due to the radial symmetry of our solution, we plot the numerical and exact solutions

along the $y = z = 0$ midline for $x \in [-5, 5]$, which gives better clarity in our comparison.

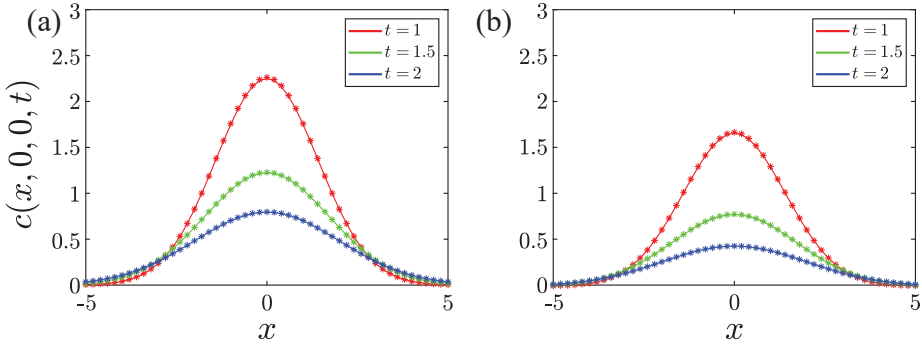


Figure 3.3: Comparison of exact (solid) and numerical (stars) solutions of Equation (3.5). All results correspond to $S = 100$ and $D = 1$, with $h = 0.2$. Results in (a) are for $\kappa = 0$, whereas results in (b) are for $\kappa = 0.3$.

3.4 Numerical method and parameters

Here we provide the discretisation for the numerical method and additional evidence to justify our choices of the numerical parameters chosen for the simulation. In summary, these choices include tolerances for the numerical solution of the linear system associated with solving Equation (2.8); the size of the domain; the time duration between solving Equation (2.8); and the spatial discretisation required to solve Equation (2.8).

3.4.1 Numerical discretisation

We solve Equation (2.8) by discretising the domain, Ω , into a uniform structured finite volume mesh with cubic finite volumes, consisting of I^3 equally-spaced nodes with node spacing h [μm]. We approximate the cell density $v(\mathbf{x}, t)$ in Equation (2.8) by the agent density, $N_{i,j,k}/h^3$, around node (x_i, y_j, z_k) , where $N_{i,j,k}$ [cells] is the number of agents inside the node's control volume, and $h = L/(I-1)$. The discretised 3D finite volume equation is

$$h(c_{i-1,j,k} + c_{i,j-1,k} + c_{i,j,k-1} + c_{i+1,j,k} + c_{i,j+1,k} + c_{i,j,k+1} - 6c_{i,j,k}) - \alpha c_{i,j,k} N_{i,j,k} = 0, \quad (3.7)$$

for the internal nodes, and $c_{i,j,k} = 1$ at boundary nodes. Assembling these discrete equations gives a linear system that we solve numerically,

$$\mathbf{A}\mathbf{c} = \mathbf{b}, \quad (3.8)$$

where $\mathbf{A} \in \mathbb{R}^{I^3 \times I^3}$ is the coefficient matrix and $\mathbf{b} \in \mathbb{R}^{I^3}$ is the right-hand side vector for Equation (3.7), and $\mathbf{c} \in \mathbb{R}^{I^3}$ is the solution.

3.4.2 GMRES tolerance

To solve Equation (3.8), we use the generalised minimal residual method (GMRES) in MATLAB [68]. Initially, we solve the linear system by assuming that $c = 1$ at all nodes and specify a strict relative tolerance ε given by,

$$\varepsilon = \frac{\|\mathbf{b} - \mathbf{A}\mathbf{c}\|}{\|\mathbf{b}\|}, \quad (3.9)$$

where $\|\cdot\|$ is the 2-norm. Once this initial solution is obtained using a strict tolerance, we find that all subsequent solutions of Equation (3.7) can

be obtained with a larger tolerance since we have an improved estimate of the solution to initialise the iterative solver.

To determine the first tolerance required to solve the linear system, ε_1 , we suppose that $c = 1$ at all nodes on a mesh with $I^3 = 201^3$ equally-spaced nodes (Section 3.4.4) and solve the resulting system with a range of ε_1 using MATLAB's `gmres` function. Table 3.1 compares the computation time as a function of ε_1 , and Figure 3.4 compares the resulting nutrient profile solutions along the midline of the domain, $y = z = 0$.

Table 3.1: Runtimes for the initial solution to Equation (3.8). Solution runtimes were achieved with high performance computing, using four 64 bit Intel Xeon core processors per simulation.

ε_1	Runtime (min.)
1×10^{-6}	0.8
1×10^{-7}	13.0
1×10^{-8}	19.3
1×10^{-9}	24.4

Approaches utilising other, more specified initial guesses were also performed, but showed no improvement on runtimes for the initial solution. Since we see that the solutions for $\varepsilon_1 = 1 \times 10^{-8}$ and 1×10^{-9} are visually indistinguishable at this scale, we always work with $\varepsilon_1 = 1 \times 10^{-8}$.

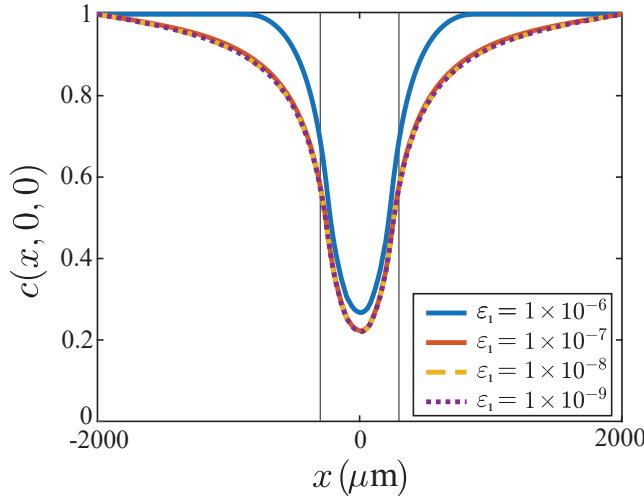


Figure 3.4: Comparison of steady-state solutions to Equation (3.7) with different values of ε_1 . Solutions with $\varepsilon_1 \leq 1 \times 10^{-8}$ are entirely visually indistinguishable, and those for a tolerance of $\varepsilon_1 = 1 \times 10^{-7}$ or lower visually match in the region occupied by the spheroid at $t = 0$ days, denoted by the vertical lines.

To update the nutrient distribution subsequently, we find that we do not need such a strict tolerance choice for subsequent solutions of Equation (3.7), ε_2 , as we have an improved estimate for the nutrient profile from the initial solution. To improve the estimate for the initial guess, we solve Equation (3.7) on a relatively coarse mesh of $I^3 = 51^3$ nodes and solve the linear system using MATLAB's left matrix division (backslash) operator [69], and then interpolate this coarse solution onto the finer $I^3 = 201^3$ mesh, which serves as an initial guess for the next GMRES solution that can be obtained with a more relaxed tolerance. Table 3.2 compares the computation time between subsequent solutions as a function of ε_2 .

Table 3.2: Runtimes for subsequent solutions to Equation (3.8). Solution runtimes were achieved with high performance computing, using four 64 bit Intel Xeon core processors per simulation.

ε_2	Runtime (min.)
1×10^{-6}	0.15
1×10^{-7}	0.95
1×10^{-8}	10.1
1×10^{-9}	20.6

Results in Figure 3.5 show $c(x, y, z)$ plotted along the midline $y = z = 0$ for one of these subsequent solutions for various choices of tolerances. Since we see that the solutions are all largely indistinguishable, and more restrictive tolerances are associated with significant increases in runtime with insignificant improvement in accuracy, we set $\varepsilon_2 = 1 \times 10^{-6}$ for all remaining calls to `gmres`.

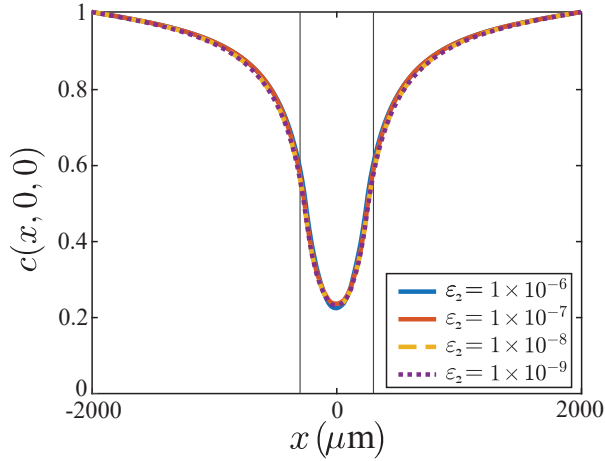


Figure 3.5: Comparison of GMRES solutions to Equation (3.7) with different values of ε_2 . When the initialisation is set to a previous solution, $\varepsilon_2 = 1 \times 10^{-6}$ is sufficient to find solutions that are visually indistinguishable from solutions with more restrictive tolerances.

3.4.3 Domain size

Another important consideration for the numerical simulation is the choice of domain size, L . We aim to choose L to be large enough that the agents do not touch the boundary during the simulations, but not so large as to incur a significant computational overhead (Figure 3.6).

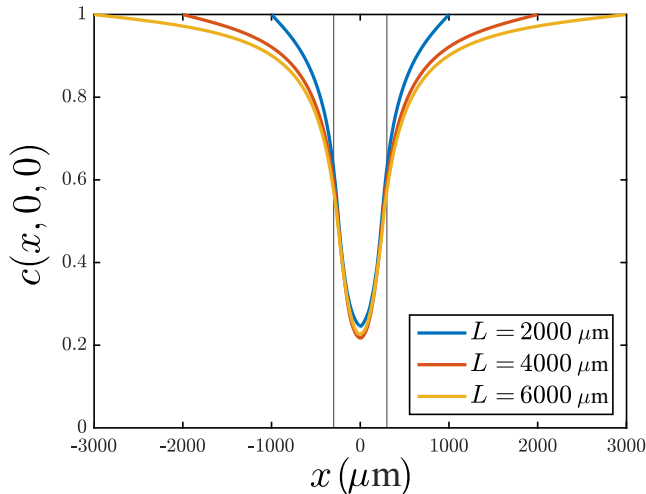


Figure 3.6: Comparison of steady-state solutions to Equation (3.7) along one dimension (x) with varying domain lengths. The vertical lines represent the region of the test spheroid.

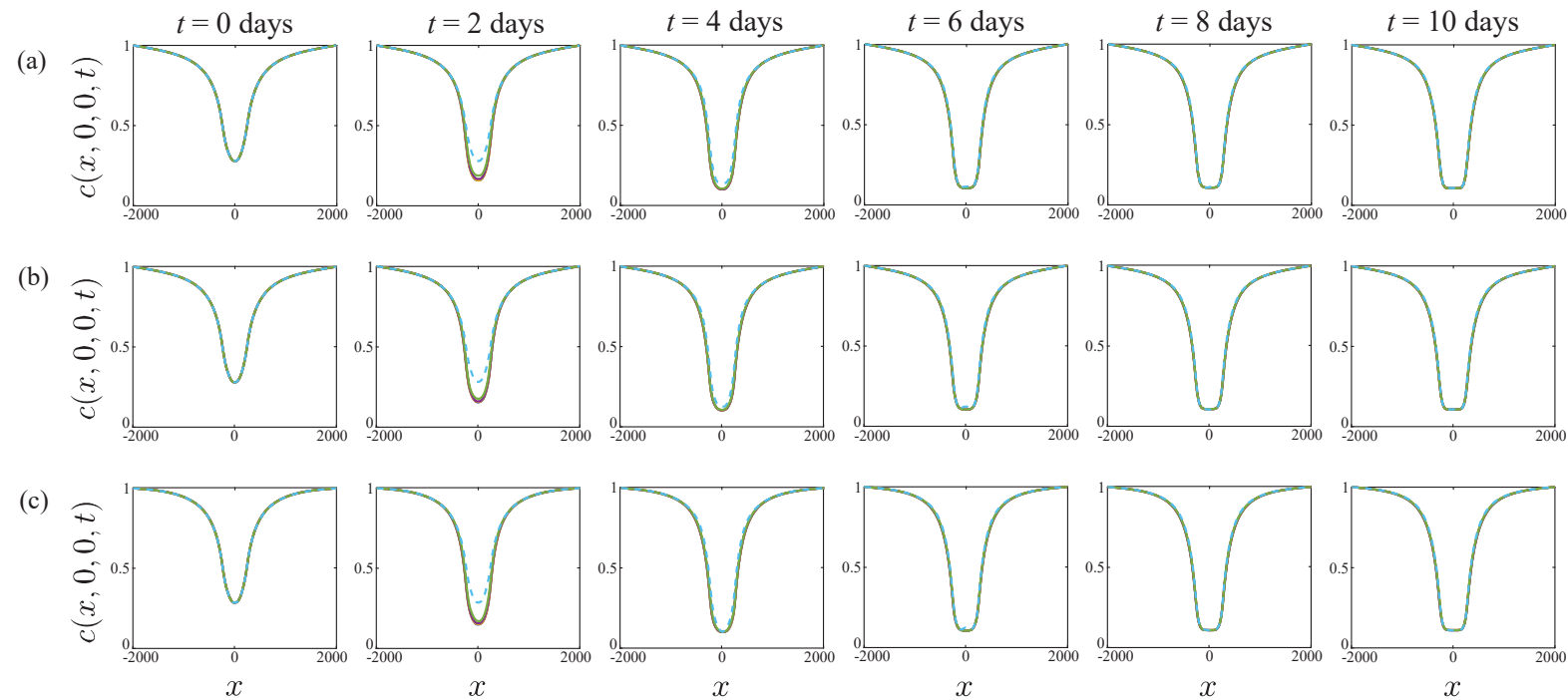


Figure 3.7: Influence of variation in I^3 and t^* on nutrient solution over time. From left to right: nutrient profile solutions for day 0, 2, 4, 6, 8, and 10. Solution profiles show comparisons at these time points for $t^* = 1 \text{ h}$ (solid yellow), $t^* = 2 \text{ h}$ (solid purple), $t^* = 6 \text{ h}$ (solid green), and $t^* = 24 \text{ h}$ (dashed cyan). Solutions are averages of 10 simulations, shown for (a) $I^3 = 101^3$, (b) $I^3 = 151^3$, and (c) $I^3 = 201^3$.

To explore the choice of L we always use the same number of nodes to discretise the nutrient equation, with $I^3 = 201^3$ equally-spaced nodes, and we set the first estimate of the solution for the GMRES algorithm to be the solution obtained by considering a different spheroid of the same radius but with a different placement of agents, similar to Section 3.4.2, so that the computational efficiency of these tests is improved. We consider the domain lengths $L = 2000$, 4000 , and $L = 6000\mu\text{m}$, and plot the resulting nutrient profiles along the midline $y = z = 0$ in Figure 3.6. While the boundary has a clear effect on the solution on the outer regions of the domain, the solutions are very similar in the region $|x| < 500\mu\text{m}$ where agents are located and nutrient is being consumed. The two solutions for $L = 4000\mu\text{m}$ and $L = 6000\mu\text{m}$ are very similar in the region of the spheroid and also its immediate vicinity. Consequently, we choose a domain length $L = 4000\mu\text{m}$.

3.4.4 Spatial and temporal resolution of the nutrient profile

There are two main considerations when we solve Equation (3.7) for the nutrient profile: first we must choose an appropriate spatial discretisation, I^3 ; second, we must choose the duration of time between solutions of Equation (3.7), t^* . Results in Figure 3.7 show the nutrient profiles along the midline $y = z = 0$ for a range of values of I^3 and t^* . The time scale for t^* is hours, as this is the most appropriate choice for simulating agent-level behaviour, but we represent the results in days as a more intuitive and natural choice for growth on the scale of the spheroids.

Profiles in Figure 3.7 indicate that the solution is relatively insensitive to the choice of I^3 , but we see a clear difference in solutions depending on the choice of t^* . The solutions in Figure 3.7 are insensitive to t^* when we choose $t^* \leq 2\text{ h}$. Estimates of combinatorial runtime in Table 3.3 show that setting $t^* < 1\text{ h}$ slows the simulations considerably. As a consequence, we choose $t^* = 1\text{ h}$.

Table 3.3: Table of average runtime data (min.) for 10 simulations with varying I^3 and t^* . The computational experimental period of these simulations is $T = 240\text{ h}$. Simulation runtimes are from high performance computing, using four 64 bit Intel Xeon core processors per simulation.

I^3	$t^* = 0.1\text{ h}$	$t^* = 0.5\text{ h}$	$t^* = 1\text{ h}$	$t^* = 2\text{ h}$	$t^* = 6\text{ h}$	$t^* = 24\text{ h}$
101^3	55.1	38.6	37.7	37.4	27.5	26.2
151^3	101.0	57.1	50.8	48.4	37.6	36.3
201^3	224.9	100.0	84.7	75.9	63.3	58.5

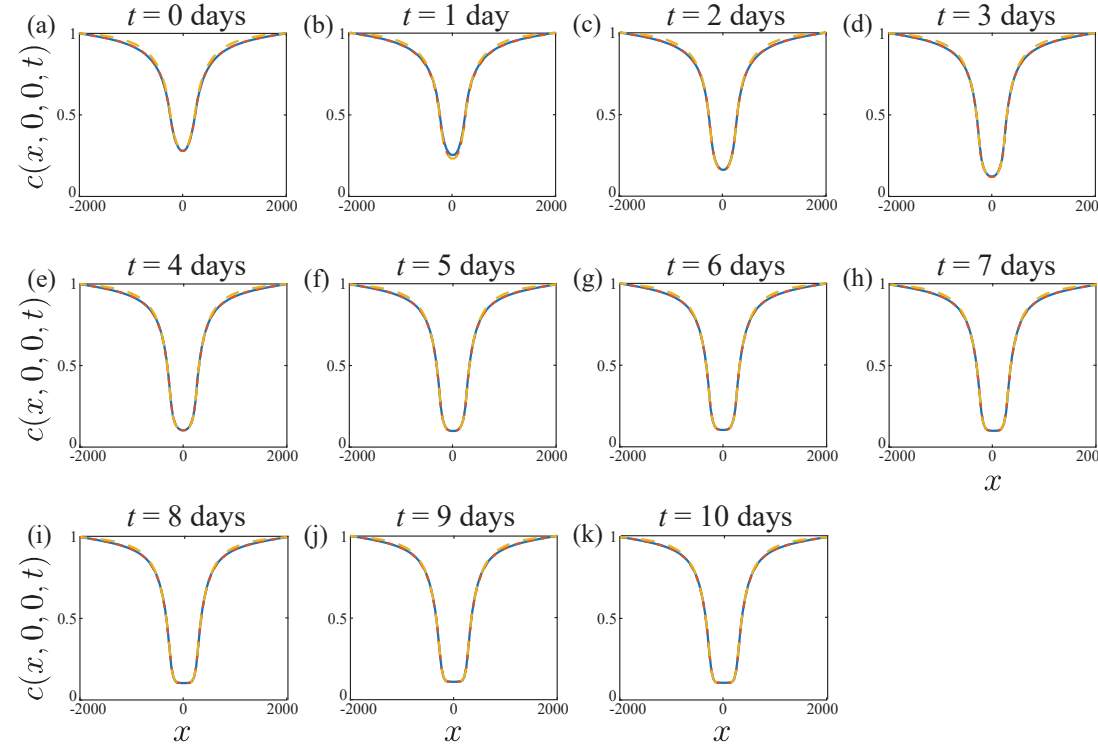


Figure 3.8: Influence of variation in I^3 when setting $t^* = 1$ h. (a)–(k) are comparisons of the solutions for $I^3 = 101^3$ (solid blue), $I^3 = 151^3$ (dashed red), and $I^3 = 201^3$ (dashed yellow) at days 0–10 respectively. As before, solutions are averages of profiles from 10 simulations.

Additional results in Figure 3.8 show solutions for various grid resolutions $I^3 = 101^3, 151^3, 201^3$ for $t^* = 1$ h. At early time we see some difference in these solutions on the coarser mesh, but the solutions for $I^3 = 151^3$ and 201^3 are visually indistinguishable at this scale. Therefore, in all simulations we set $t^* = 1$ h and $I^3 = 201^3$.

3.5 Estimation of cell diameter

To reduce the number of unknown input parameters for the numerical experiments, we fix the experimental cell diameter Δ , which in turn informs the proliferation and migration step size, σ and μ , respectively [48].

WM793B cells were stained with $10 \mu\text{M}$ CellTracker™ [70], at a density of 1×10^6 cells in $100 \mu\text{L}$ of tracker solution. After spinning the cell suspension at 300 relative centrifugal force for 2 minutes in a centrifuge, the CellTracker solution was removed and the pellet resuspended in 5 mL of growth medium. The cell suspension was spun down, before removal of the growth medium and resuspension of the stained cells in a solution of 2% low melting agarose in phosphate buffered solution (PBS). The solution was mounted on a chamber slide for preparation for imaging (Figure 3.9a). Images of the cell size were taken with a 20x Olympus UPlanSApo objective, where the Z range was set so that it was large enough to encompass a large sample of cells for analysis. Quantitative estimates of the WM793B cell size were achieved through computational image analysis with Fiji (ImageJ) software [71], using the 3D Cell Counter function to calculate the volume of the cells lying in the Z range.

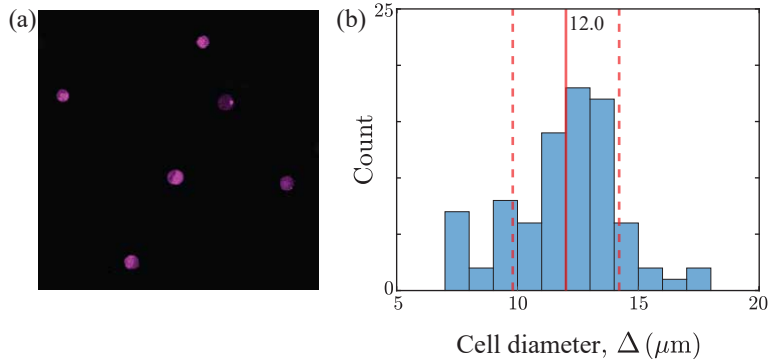


Figure 3.9: Estimation of the cell diameter for the WM793B cell line. (a) A visualisation of part of the window at one of the 50 Z heights, showing the equators of some of the suspended cells in the sample. The region identified with magenta colouring represents the entire cell. (b) Distribution of cell diameters from calculated volumes of the objects in the imaged volume. The solid line is the average diameter, and dashed lines represent one standard deviation from this average.

The 3D volume calculated by ImageJ is converted into an equivalent diameter of a sphere, giving $\Delta = 12.0 \mu\text{m}$ by taking the sample mean from 84 objects, distributed as shown in Figure 3.9b.

3.6 Estimation of cell cycle progression rates

We repeat the procedure for cell cycle duration estimates from [5] for the WM793b cell line. To estimate the maximum G1-early S phase (G1-eS) cycling rate R_r , the constant eS-S/G2/M cycling rate R_y , and the constant S/G2/M mitosis rate R_g , we use a series of 2D experiments as follows. The WM793B melanoma cells were seeded into a 12 well (3.82 cm^2 per well) #1.5 glass bottom plate, at a seeding density of 40 000 cells per well, and covered with 1 mL of growth medium, prepared as in [2]. The 2D cell culture was imaged in a Zeiss AxioObserver (Zeiss, Oberkochen, Germany) every 5 minutes for a period of 72 h, allowing for at least one full cell cycle to be completed. Then, 30 cells were tracked from the point of cell division through a full cell cycle, and the duration spent in each phase was measured and recorded. An example case of the fluorescence exhibited by individual cells in the two-dimensional assay is shown in Figure 3.10a.

Our measurements suggest that the average time spent in each stage of the cell cycle is $t_r = 21.3 \text{ h}$ in red, $t_y = 2.0 \text{ h}$ in yellow, and $t_g = 16.2 \text{ h}$ in green. The progression rates are the reciprocals of these values, giving values of $R_r = 0.047 / \text{h}$, $R_y = 0.50 / \text{h}$, and $R_g = 0.062 / \text{h}$, which are the values for cell cycle progression that we use in the model. Figure 3.10b shows the time spent in the different phases of the cell cycle for each phase, with the mean and one standard deviation indicated.

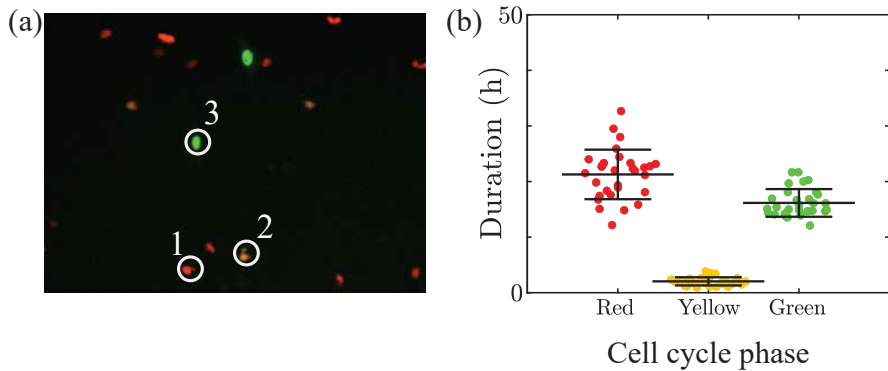


Figure 3.10: Estimation of the time spent in different stages of the cell cycle. (a) A section of one of the windows, indicating the visualisation and colourisation of the acquired FUCCI cell images. Examples of a red (1), yellow (2), and green (3) cell, where the yellow colour is generated by a composite of emission in the red and green channel. (b) A swarm chart of the duration of red, yellow, and green stages for 30 individual observations. Bars are mean \pm standard deviation.

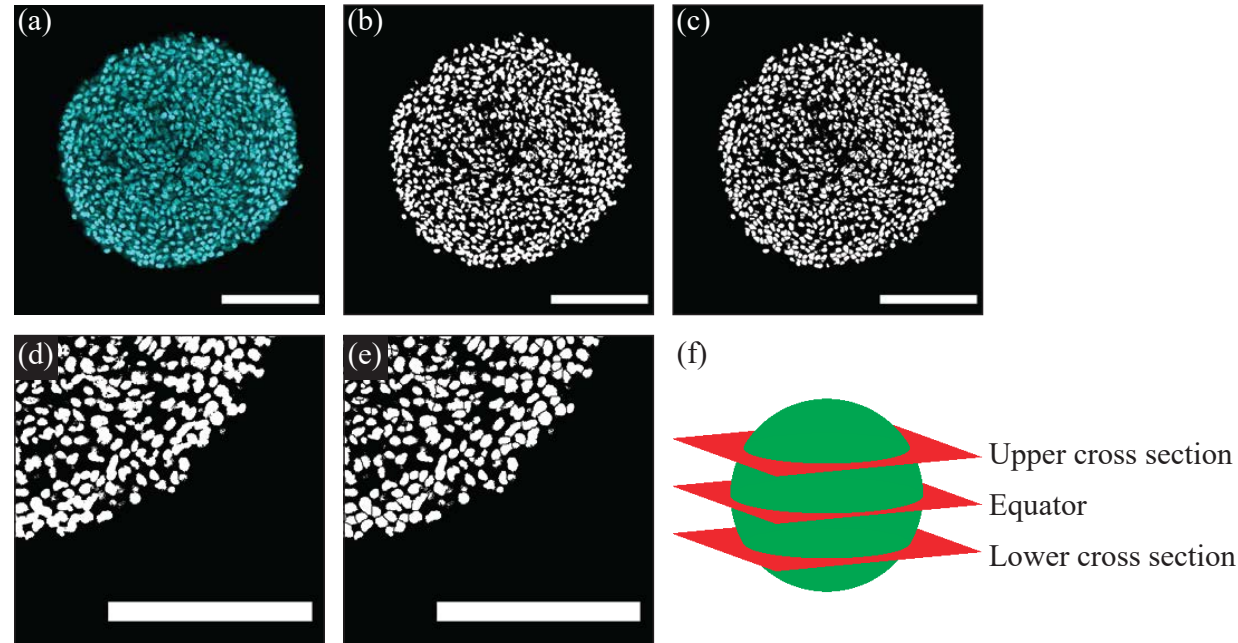


Figure 3.11: Demonstration of the process for preparing spheroid images for analysis. The spheroid is (a) imported into ImageJ, (b) binarised, and (c) watershed processed. (d)-(e) A zoomed-in demonstration showing the spheroid (d) before processing with watershed and (e) after processing with watershed. (f) Representation of the locations of the upper cross section, equator and lower cross section. Scale bars represent 200 μm .

3.7 Initial cell number

Using the 3D experimental images, we estimate the initial cell count in the spheroid using FIJI (ImageJ) software [71] analysis of images at three different heights in the spheroid at $t = 0$ days. Once the image is loaded into ImageJ (Figure 3.11a), the image is binarised (Figure 3.11b) so that all pixels below a brightness threshold are black, and all above the threshold are white. Then, the watershed feature is used to segment connected groups of objects in the image, so that they may be counted properly (see Figure 3.11c-e). The finalised image is then processed with the Analyse Particles function, where the minimum size for an object is mandated to avoid counting residual pixels from the background removal. The minimum area for a cell was set at $25 \mu\text{m}^2$. No maximum threshold was set, as experimentation with this parameter showed that it had a negligible effect on the cell count.

The area of the cells in the 2D image was recorded along with the cell count. Using the estimate of the cell diameter of $12 \mu\text{m}$ (from Section 3.5), and assuming the density of cells in the slice area is the same as the volume density of cells in the entire spheroid, we obtain an approximate count of the cells in the spheroid at $t = 0$ days. This process was applied to images from the equator, and one from halfway to the top or bottom of the spheroid, labelled as the upper and lower cross sections (see Figure 3.11f). Two different spheroids at $t = 0$ days are used to estimate the total cell number at formation. Results (Table 3.4) indicate that spheroids at $t = 0$ days are composed of approximately $27\,000 - 31\,000$ cells per spheroid. For simplicity, we simulate spheroids with $30\,000$ cells per spheroid at $t = 0$ days.

Table 3.4: Measurements of spheroid geometry and number of cells. Numbers in brackets in column 1 indicate the spheroid replicate imaged in 3D.

Image location	Area (μm^2)	Radius (μm)	Volume (μm^3)	Cell count (2D area)	Density (%)	Cell count (3D volume)
Equator (1)	1.58×10^5	224.24	4.72×10^7	739	52.91	27619
Upper cross sect. (1)	1.18×10^5	193.77	4.72×10^7	542	51.97	27128
Lower cross sect. (1)	1.14×10^5	190.15	4.72×10^7	511	50.88	26560
Equator (3)	1.84×10^5	242.24	5.95×10^7	766	46.99	30926
Upper cross sect. (3)	1.07×10^5	184.22	5.95×10^7	449	47.63	31343
Lower cross sect. (3)	1.58×10^5	223.94	5.95×10^7	643	46.16	30376

3.8 Initialising the IBM

Here we describe how we choose the initial proportion of red, yellow, and green agents in each simulation. Results in Section 3.6, show that the average time a cell spends in each phase of the cell cycle is $t_r = 21.3$ h (red), $t_y = 2.0$ h (yellow), and $t_g = 16.2$ h (green). Therefore, we assume that the total cell cycle time is

$$t_c = t_r + t_y + t_g. \quad (3.10)$$

We then define various population proportions $\beta_r = t_r/t_c$, $\beta_y = t_y/t_c$, and $\beta_g = t_g/t_c$, for red, yellow, and green agents, respectively.

In the freely-cycling region of a spheroid, $r_a(t) < r < r_o(t)$, we distribute agent numbers according to these proportions. Since $\beta_r + \beta_y + \beta_g = 1$, we can form a cumulative distribution of these agent proportions. For each agent, we sample a uniform random number $u_1 \in [0, 1]$, and perform inverse transform sampling on our cumulative distribution created by our population proportions, such that the agent is red if $u_1 < \beta_r$, yellow if $u_1 \in [\beta_r, \beta_r + \beta_y]$, and green otherwise (Figure 3.12a).

Experimentally, we see an initial arrested radius $r_a(0) > 0$, meaning that the intensity of yellow and green for $r < r_a(0)$ is less than 20% (Section 3.2). Since we assume that G1-arrest is associated with low nutrient availability, we reduce the proportion of yellow and green agents to 16% of the population in the region where $c(\mathbf{x}, 0) < c_a$, with the remaining 84% of the population specified to be red. Our choice of 16% is selected from a series of screening simulations that show this choice provides a good match to early experimental measurements. The algorithm implementing this approach is similar to that applied to agents in the freely-cycling region. For each agent with $c(\mathbf{x}, 0) < c_a$ the agent is red with probability 0.84 (Figure 3.12b). Otherwise, we sample a uniform random number $u_2 \in [0, 1]$. Since we assume that commitment to the cell cycle (progression from G1 phase to eS phase) frees an agent from reliance on the local nutrient concentration, we expect that the yellow and green agents will be proportional to their cell cycle durations in this final 16% of the population, so that

$$\zeta_y = \frac{t_y}{t_y + t_g} \quad (3.11)$$

is the proportion of the remaining 16% that is taken up by yellow agents,

and

$$\zeta_g = \frac{t_g}{t_y + t_g} \quad (3.12)$$

is the proportion of the 16% taken up by green agents. Hence, the agent is yellow if $u_2 < \zeta_y$, and green otherwise (Figure 3.12b). Overall, we find that this experimentally-motivated approach to initialise our IBM simulations leads to a good match between simulated estimates of $r_a(t)$ and our experimental measurements. Of course, if the IBM were applied to a model of 4D tumour spheroids with a different cell line, we anticipate that this approach would be valid, but that new measurements of t_r , t_y , and t_g would be required to apply this method.

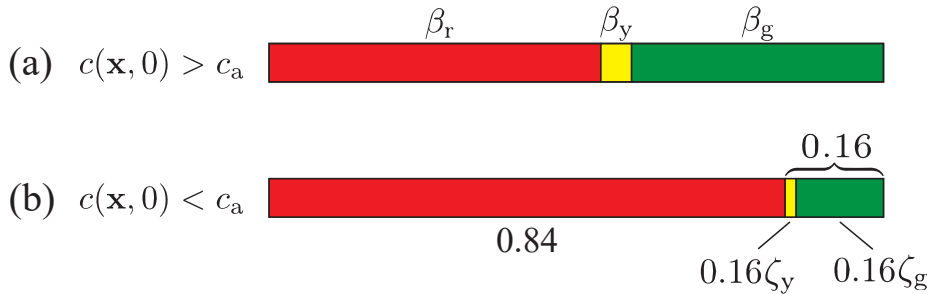


Figure 3.12: Representation of initial agent cell cycle stage proportions in (a) the freely-cycling region ($c(\mathbf{x}, 0) > c_a$) and (b) the region of restricted nutrient concentration ($c(\mathbf{x}, 0) < c_a$). In the freely-cycling region in (a), subpopulation proportions are set strictly by the proportions of time spent in each phase of the cell cycle, β_r for red agents, β_y for yellow agents, and β_g for green agents. In the region of restricted nutrient concentration in (b), the best qualitative match to experimental data is when red agents make up 84% of the population, and the remaining 16% is partitioned between yellow and green with proportions ζ_y and ζ_g , respectively.

3.9 Simulation algorithms

Here, we describe pseudo-algorithms for the IBM, where Algorithm 1 solves the nutrient concentration with MATLAB code, and calls Algorithm 2 to calculate the agent-level behaviours with code in C.

Algorithm 1: A single realisation of the IBM, from $t = 0$ h to $t = T$ h.

- 1 Set parameter values from function inputs, $\theta = (N(0), L, r, \sigma, \mu, T, t^*, R_r, R_y, R_g, d_{\max}, d_{\min}, m_{\max}, m_{\min}, \eta_1, \eta_2, \eta_3, I, \alpha, c_b, c_a, c_m, c_d)$
 - 2 Establish an I^3 equally-spaced finite volume mesh grid for the steady-state nutrient profile
 - 3 Set $N(0)$ random initial agent locations within a sphere of radius r
 - 4 Set $t = 0$
 - 5 Solve the linear system of Equation (3.7) for the initial agent density C with MATLAB's inbuilt GMRES function [68], setting $\text{tol} = 1 \times 10^{-8}$ (ε_1) and an initial guess of $c = 1$ at all nodes (Section 3.4.2)
 - 6 Calculate the nutrient concentrations from the mesh at the agent locations with linear interpolation
 - 7 Assign each agent a cell cycle status (red, yellow, green), and record $N_r(0)$, $N_y(0)$, and $N_g(0)$ (Section 3.8)
 - 8 Calculate nutrient-dependent rates $R_r(c)$, $m(c)$, and $d(c)$ for all agents from Equation (2.1), Equation (2.4), and Equation (2.5)
 - 9 **while** $t < T$
 - 10 Set $t = t + t^*$
 - 11 Solve the steady-state system of Equation (3.7) with the current spheroid agent locations with MATLAB's inbuilt GMRES function, setting $\text{tol} = 1 \times 10^{-6}$ (ε_2) and an initial guess of c_p , where c_p is the previous steady-state solution (Section 3.4.2)
 - 12 Update c_n for each agent with trilinear interpolation
 - 13 Resolve the cell events (Algorithm 2)
 - 14 **end**
-

Algorithm 2: The Gillespie algorithm for simulating migration, cell cycle progression, and death.

```

1 Set inner timer  $t_{in} = 0$ 
2 while  $t_{in} < t^*$ 
3    $d_t = \sum_{n=1}^{N(t)} (d(c))_n$ ,  $m_t = \sum_{n=1}^{N(t)} (m(c))_n$ ,
    $R_t = \sum_{n=1}^{N_r(t)} (R_r(c))_n + N_y(t)R_y + N_g(t)R_g$ 
4   Calculate the total rate of events  $\lambda = d_t + m_t + R_t$ 
5   Sample the Gillespie time step to the next event  $\tau \sim \text{Exp}(\lambda)$ 
6   Set  $t_{in} = t_{in} + \tau$ 
7   Perform an event, with cycling probability  $R_t/\lambda$ , migration probability
       $m_{tot}/\lambda$ , and death probability  $d_{tot}/\lambda$ 
8   if cycling event
9     Sample agent  $n$  to continue through the cell cycle, with probability
       proportional to its cycling rate
10    if the agent is red
11      Turn the agent yellow
12       $N_r = N_r - 1$ ,  $N_y = N_y + 1$ 
13      Set the  $n$ th agent's cycling rate to  $R_y$ 
14    else if the agent is yellow
15      Turn the agent green
16       $N_y = N_y - 1$ ,  $N_g = N_g + 1$ 
17      Set the  $n$ th agent's cycling rate to  $R_g$ 
18    else if the agent is green
19      Turn the agent red
20      Set  $\theta = 2\pi u_1$ ,  $\varphi = \arccos(1 - 2u_2)$ ;  $u_1, u_2 \sim \mathcal{U}(0, 1)$ 
21       $x_n = x_n + \sigma/2 \cos(\theta) \sin(\varphi)$ ,  $y_n = y_n + \sigma/2 \sin(\theta) \sin(\varphi)$ ,
          $z_n = z_n + \sigma/2 \cos(\varphi)$ 
22       $x_{\text{new}} = x_n - \sigma/2 \cos(\theta) \sin(\varphi)$ ,  $y_{\text{new}} = y_n - \sigma/2 \sin(\theta) \sin(\varphi)$ ,
          $z_{\text{new}} = z_n - \sigma/2 \cos(\varphi)$ 
23       $N_g = N_g - 1$ ,  $N_r = N_r + 2$ 
24      Interpolate the nutrient concentrations to both new locations
25      Set  $R_r(c)$ ,  $m(c)$ , and  $d(c)$  for both new agents according to Equation
         (2.1), Equation (2.4), and Equation (2.5)
26      Adjust the population count in the agents' control volumes
27  end
28 else if migration event
29   Sample agent  $n$  to migrate, with probability proportional to its
      migration rate
30   Set  $\theta = 2\pi u_1$ ,  $\varphi = \arccos(1 - 2u_2)$ ;  $u_1, u_2 \sim \mathcal{U}(0, 1)$ 
31    $x_n = x_n + \mu \cos(\theta) \sin(\varphi)$ ,  $y_n = y_n + \mu \sin(\theta) \sin(\varphi)$ ,  $z_n = z_n + \mu \cos(\varphi)$ 
32   Interpolate the nutrient concentration at the new location  $\mathbf{x}_n$ 
33   Set  $R_r(c)$ ,  $m(c)$ , and  $d(c)$  for the agent at its new location with
      Equation (2.1), Equation (2.4), and Equation (2.5)
34   Account for changes to populations in control volumes, if necessary
35 else if death event
36   Sample an agent to die, with probability proportional to its death rate
37    $N = N - 1$ 
38   Remove the agent from the simulation, and move it to the dead
      population
39 end
40 end
```

3.10 Calculation of agent density profiles

Here, we describe the procedure to estimate the profiles of relative agent densities as functions of distance from the periphery in Figure 2.4c. At a given time, t , we select the largest outer radius from all simulations, measured with image processing (Section 3.2). We then calculate the largest multiple of $10 \mu\text{m}$ that is less than this selected radius, and denote this r_{\max} . For example, if at time t the outer radii from all simulations are $r_o(t) = 247, 248, 249, 251$, and $252 \mu\text{m}$, the largest outer radius is $r_o(t) = 252 \mu\text{m}$, and we choose $r_{\max} = 250 \mu\text{m}$. This choice of r_{\max} ensures that the bin corresponding to the largest radial distance does not include space beyond the spheroid periphery, and this is reasonable as, for 10 identically-prepared simulations, the variability in $r_o(t)$ is less than 1% (Figure 2.8).

We partition the interval $[0, r_{\max}]$ into bins of width $w = 10 \mu\text{m}$, which we find is sufficiently small to capture the spatial evolution of agent density, but is also sufficiently large to avoid excessive fluctuations [65]. The bins representing radial position are converted into bins representing distance from the periphery with the transformation,

$$\mathbf{p}_b = \mathbf{r}_{\max} - \mathbf{r}_b, \quad (3.13)$$

where $\mathbf{r}_{\max} [\mu\text{m}]$ is a vector with all elements equal to r_{\max} and length equal to the number of bin edges, and $\mathbf{r}_b [\mu\text{m}]$ and $\mathbf{p}_b [\mu\text{m}]$ are the locations of the bin edges for the radial distance and the distance to the periphery, respectively (Figure 3.13a).

We now demonstrate the calculation of the relative agent density distributions, using the green agents as an example, but the calculation is identical for the other agent types. First, all 3D Cartesian agent locations in a given simulation at t are imported. We calculate the radial coordinate of the n th green agent, r_n , as the Euclidean distance from its 3D Cartesian coordinate, \mathbf{x}_n , to the mean location of all agents of all types at time t , $\bar{\mathbf{x}}(t)$, such that

$$r_n = \|\mathbf{x}_n - \bar{\mathbf{x}}(t)\|, \quad n = 1, \dots, N_g(t), \quad (3.14)$$

where $N_g(t)$ is the number of green agents at time t . Assuming spherical symmetry, the distance to the spheroid periphery, $p_n(t)$, is calculated by subtracting r_n from the outer radius, $r_o(t)$,

$$p_n(t) = r_o(t) - r_n, \quad n = 1, \dots, N_g(t), \quad (3.15)$$

where $p_n(t)$ is explicitly time-dependent through $r_o(t)$. This calculation of the distance to the periphery for all green agents at time t in a particular simulation is then repeated for all 10 simulations, and the sample means and standard deviations for these counts in each bin are calculated.

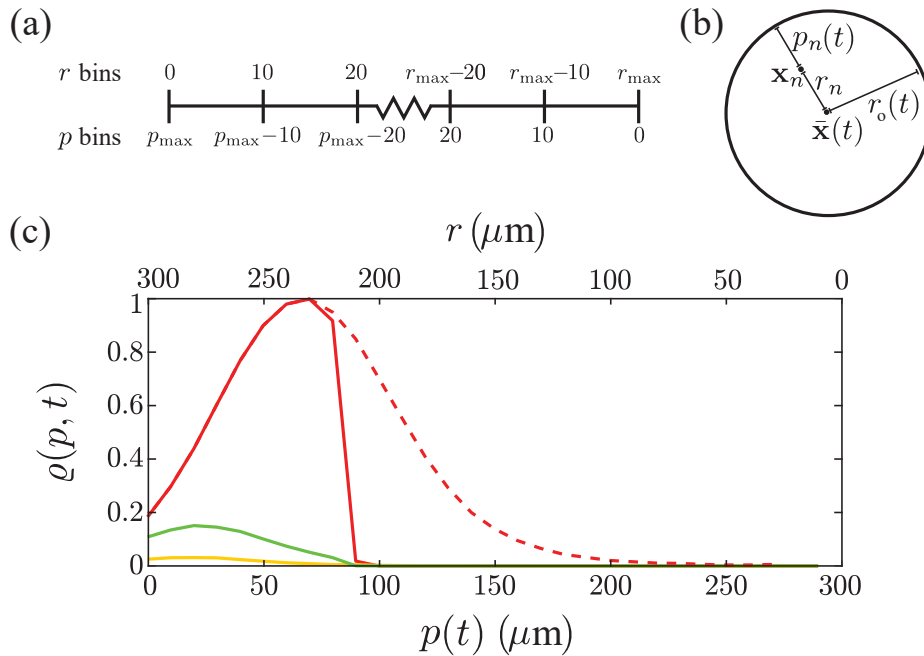


Figure 3.13: Schematic representation of the radial and distance to the periphery calculations. (a) The partitioning of bins for radial distance, and the associated bins for the distance to the periphery, calculated from the transformation in Equation (3.13). (b) Demonstration of the positional calculations for radial coordinate and distance to the periphery under the assumption of spherical symmetry. An agent located at \mathbf{x}_n within a spheroid at time t with radius $r_o(t)$ has its radial coordinate, r_n , calculated as the Euclidean distance to the average position of all agents, $\bar{\mathbf{x}}(t)$. This is then converted into the agent's distance from the periphery, $p_n(t)$, calculated from the transformation in Equation (3.15) under the assumption of spherical symmetry. (c) An example plot of the relative agent density distributions, $\varrho(p, t)$, with the distance to the periphery on the lower axis, and the corresponding radial coordinate r on the upper axis. We show example distributions of the cycling G1 (solid red), G1-arrested (dashed red), eS (yellow), and S/G2/M (green) relative agent densities.

We convert the average population counts by distance to the periphery, $C(p_l, t)$, into an agent density profile, $P(p_l, t)$ by dividing by the concentric

spherical shell volume,

$$P(p_l, t) = \frac{3C(p_l, t)}{4\pi \left(\left(r_l + \frac{w}{2} \right)^3 - \left(r_l - \frac{w}{2} \right)^3 \right)}, \quad l = 0, \dots, l_{\max}, \quad (3.16)$$

where p_l and r_l are the centres of the l th bin for distance from the periphery and radius, respectively, and $l_{\max} = r_{\max}/w - 1$ is the number of bins. We then repeat the full procedure for the other agent types (cycling red, arrested red, yellow) to calculate the average agent density profiles for all agent types at t . We then repeat the calculation of r_{\max} , \mathbf{p}_b , and density profiles for all agents at other values of t . All agent density profiles at all values of t are then normalised with respect to a maximum density, ϱ_{\max} , so that, for each agent type,

$$\varrho(p_l, t) = \frac{P(p_l, t)}{P_{\max}}, \quad l = 0, \dots, l_{\max}, \quad (3.17)$$

where P_{\max} is determined as the highest density of any type of agent over all values of t . This normalisation then gives the relative agent densities profiles, $\varrho(p, t)$ (Figure 3.13c), which are plotted in Figure 2.4c at their corresponding time points.

3.11 Sensitivity analysis

Here we outline a collection of additional results to demonstrate the sensitivity of the model to the adjustment of a number of parameters. In this section, we adjust m_{\max} and m_{\min} , d_{\max} , and η_1 . For m_{\max} and m_{\min} , we adjust them such that their ratio remains constant at $m_{\max}/m_{\min} = 2$. We choose not to adjust d_{\min} with d_{\max} , as the parameter d_{\min} represents a background death rate, whereas d_{\max} bears more significance to the model dynamics of the necrotic core. All other parameters are kept as presented in Table 2.1. We choose these parameters in particular, as these govern key elements of the quantitative behaviour of the spheroids.

3.11.1 Migration rates

Figure 3.14 shows how doubling or halving m_{\max} , with $m_{\max}/m_{\min} = 2$, influences the evolution of $r_o(t)$, $r_a(t)$, and $r_n(t)$. As we might anticipate, $r_o(t)$ increases with m_{\max} , but the trends in the sensitivity of $r_a(t)$ and $r_n(t)$ are less clear.

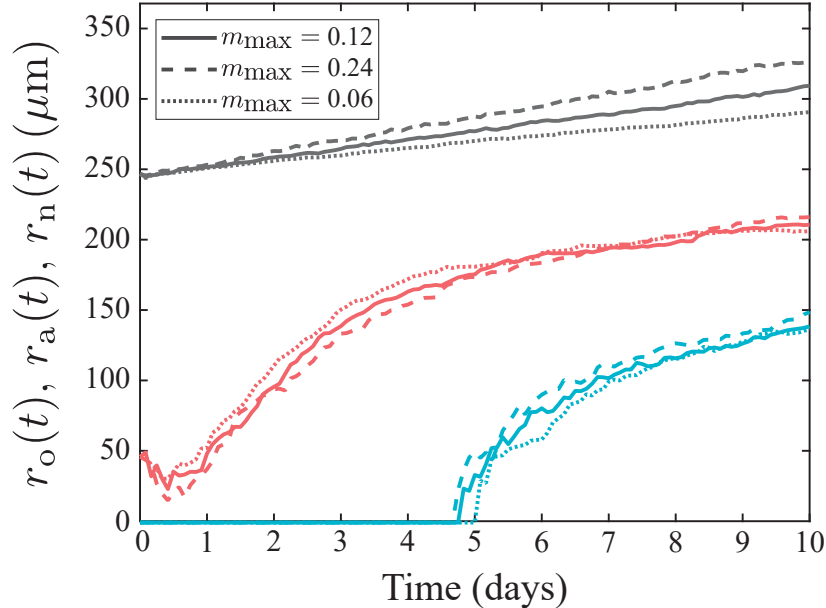


Figure 3.14: Single realisations of spheroid growth simulations with changes to m_{\max} and m_{\min} , where the ratio between the two is kept constant at $m_{\max}/m_{\min} = 2$. Evolution of $r_o(t)$, $r_a(t)$, and $r_n(t)$ is shown for the movement rates used in the model, $m_{\max} = 0.12$ (solid line), as well as for $m_{\max} = 0.24$ (dashed line) and $m_{\max} = 0.06$ (dotted line).

3.11.2 Maximum death rate

Figure 3.15 shows how doubling or halving d_{\max} affects the evolution of the radius estimates $r_o(t)$, $r_a(t)$, and $r_n(t)$. It is unsurprising that there is little effect, if any, present on $r_o(t)$ and $r_a(t)$, but there is a mild effect present on $r_n(t)$, where a higher maximum death rate corresponds to a slightly larger necrotic core, and a slightly smaller necrotic core results from a lower maximum death rate.

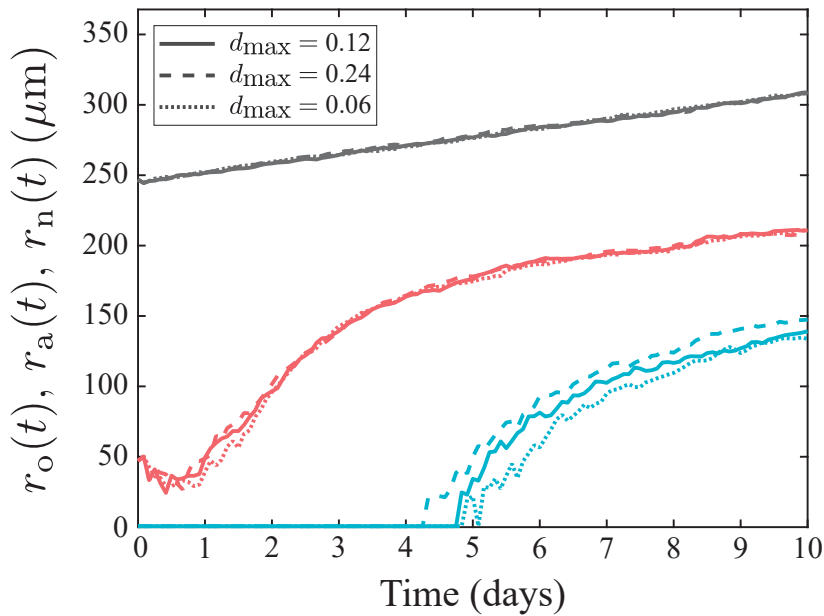


Figure 3.15: Single realisations of spheroid growth simulations with changes to d_{\max} . Evolution of $r_o(t)$, $r_a(t)$, and $r_n(t)$ is shown for the death rate used in the model, $d_{\max} = 2$ (solid line), as well as for $d_{\max} = 4$ (dashed line) and $d_{\max} = 1$ (dotted line).

3.11.3 Hill function index for arrest

In Figure 3.16, we observe the effect of changes in the Hill index, η_1 , for the response of the G1-eS transition rate to the local nutrient concentration, Equation (2.1). As we might expect, a higher η_1 corresponds with a larger $r_a(t)$, as the stricter Hill function reduces the G1-eS rate of agents. We have $r_a(0)$ consistently set for all cases (Section 3.8), but $r_a(t)$ quickly vanishes for the case where $\eta_1 = 2$ as the arrest rate is increased with a more relaxed Hill function. We see the opposite effect for $r_o(t)$, since as agents proliferate more freely when $\eta_1 = 2$, the population increases significantly and so nutrient competition is highest. In contrast, as $\eta_1 = 10$ restricts

the proliferation of agents, competition is lower and a necrotic core is less significant. To see these effects in more detail, we plot equatorial slices of the spheroids at $t = 10$ days in Figure 3.17. We can qualitatively confirm in Figure 3.17b that yellow (eS) and green (S/G2/M) agents are exclusive to the extreme periphery and the necrotic core is small, whereas Figure 3.17c shows a significant population of cycling agents entirely through to the inflated necrotic core.

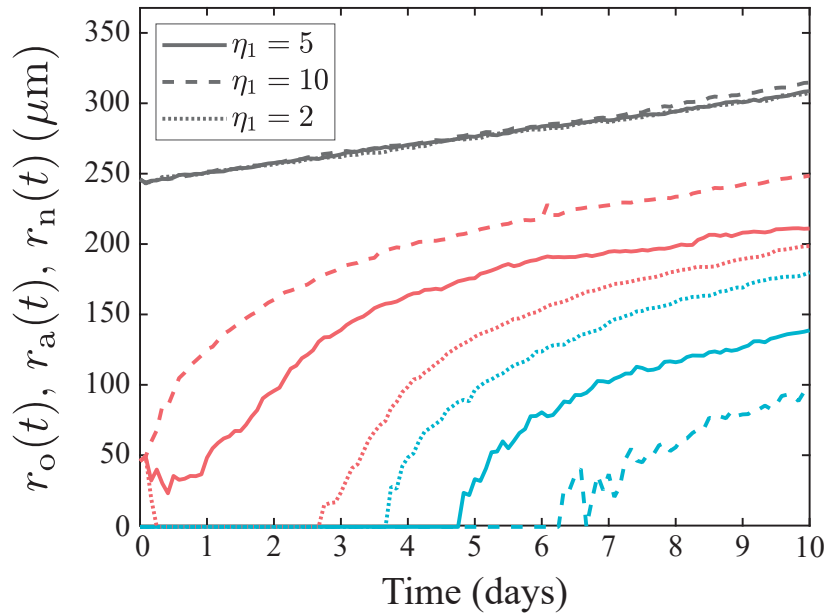


Figure 3.16: Single spheroid growth simulations realised, with changes to η_1 . The evolution of $r_o(t)$, $r_a(t)$, and $r_n(t)$ is shown for Hill index used in the model, $\eta_1 = 5$ (solid line), as well as for $\eta_1 = 10$ (dashed line) and $\eta_1 = 2$ (dotted line).

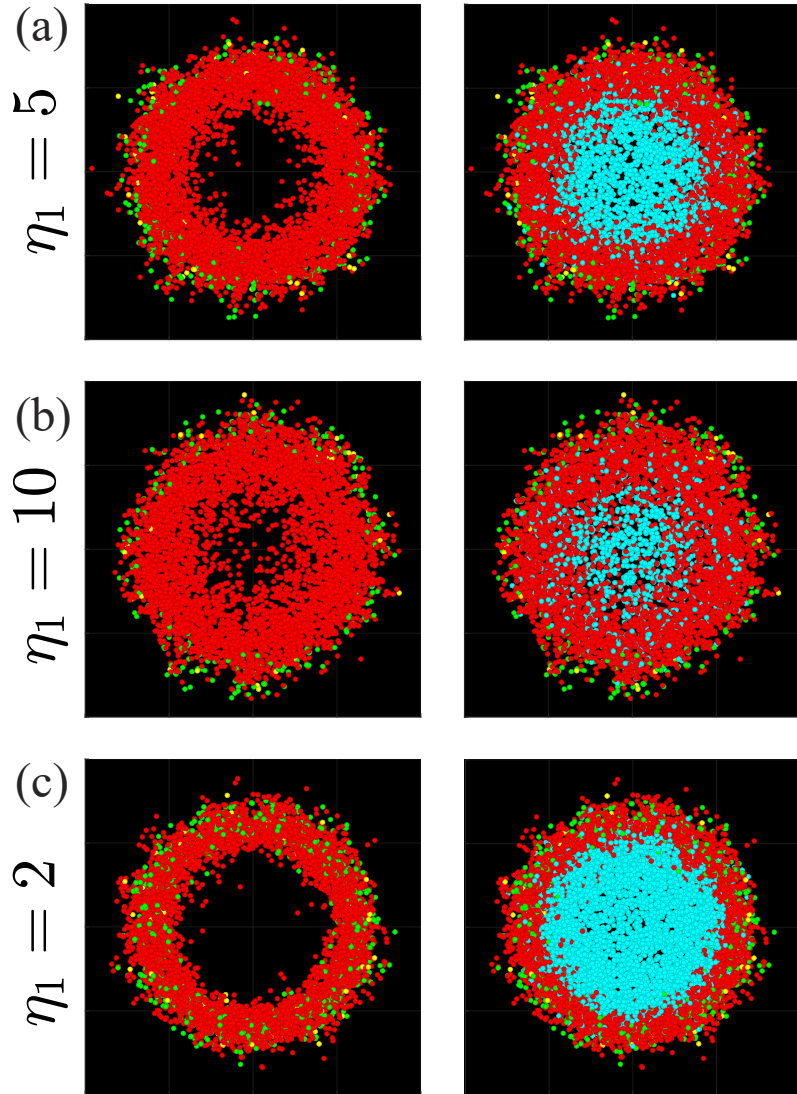


Figure 3.17: Equatorial slices of spheroids at $t = 10$ days with (a) $\eta_1 = 5$ (used in the model in Chapter 2), (b) $\eta_1 = 10$, and (c) $\eta_1 = 2$. Spheroid equators are plotted without (left) and with (right) dead agents (cyan).

The IBM requires the specification of 25 parameters and here we have shown how to explore the sensitivity of several of these parameters. We expect that similar explorations of adjustments to other assumed parameters in Table 2.1 will have reasonably similar effects to those chosen in this section. These parameters could possibly be estimated by a series of experimental tests, measuring the rates of G1-eS transition, migration and death at various levels of nutrient availability. These experiments could also inform other parameters, such as the Hill indices η_1 , η_2 , and η_3 , and

possibly even the critical concentrations c_a , c_m , and c_d .

The algorithms provided on GitHub can be used to extend this sensitivity analysis by varying any of the other parameters in conjunction with each other, and we leave this for future exploration.

3.12 Non-uniform nutrient delivery

For completeness, we now consider a simple extension of the IBM results in Chapter 2 where nutrient delivery is non-uniform. We achieve this by including a line source parallel to the y -axis at $x = 320 \mu\text{m}$, $z = 0$, which could be thought to be a very simple way to mimic nutrient delivery from a blood vessel *in vivo*. To explore this we revisit Equation (2.7) and include an additional source term which delivers nutrient at a rate that is proportional to the difference between the maximum far-field concentration and the local concentration, with proportionality constant $H > 0$, giving

$$\frac{\partial c}{\partial t} = D\nabla^2 c - \kappa cv + H(1 - c), \quad (3.18)$$

where H [/ h] can be thought of as a measure of the blood vessel permeability, and we recall that the dimensionless far-field concentration in Equation (2.7) is unity. Invoking the same steady-state approximation as before, we obtain

$$0 = \nabla^2 c - \alpha cv + \frac{H}{D}(1 - c). \quad (3.19)$$

Consequently, the new discretised 3D finite volume equation is

$$0 = h(c_{i-1,j,k} + c_{i,j-1,k} + c_{i,j,k-1} + c_{i+1,j,k} + c_{i,j+1,k} + c_{i,j,k+1} - 6c_{i,j,k}) - \alpha c_{i,j,k} N_{i,j,k} + \frac{H_{i,j,k} h^3}{D}(1 - c_{i,j,k}), \quad (3.20)$$

for the internal nodes, and $c_{i,j,k} = 1$ at boundary nodes. For all nodes that lie on the blood vessel we set $H_{i,j,k} = H > 0$, and $H_{i,j,k} = 0$ for all other nodes. In this framework we investigate a series of computational experiments with different values of H , with the other parameters as reported in Table 2.1. In Figures 3.18–3.21, we show snapshots of various spheroids, showing the distribution of agents and nutrients at the equator, at $t = 0, 3, 6$ and 10 days, respectively. Each simulation includes oxygen delivered by a blood vessel, indicated by a vertical grey line, at $x = 320 \mu\text{m}$, $z = 0 \mu\text{m}$, with $H = 1 \times 10^{-3} D / \text{h}$, $H = 5 \times 10^{-3} D / \text{h}$, and $H = 1 \times 10^{-2} D / \text{h}$. Visual inspection of these snapshots shows that the spheroids evolve with a higher density of agents in the region of the spheroid that is closest to the blood vessel, and the non-uniform distribution of agents becomes increasingly pronounced as H increases. Similarly, we see a clear asymmetry in the distribution of nutrients in these snapshots.

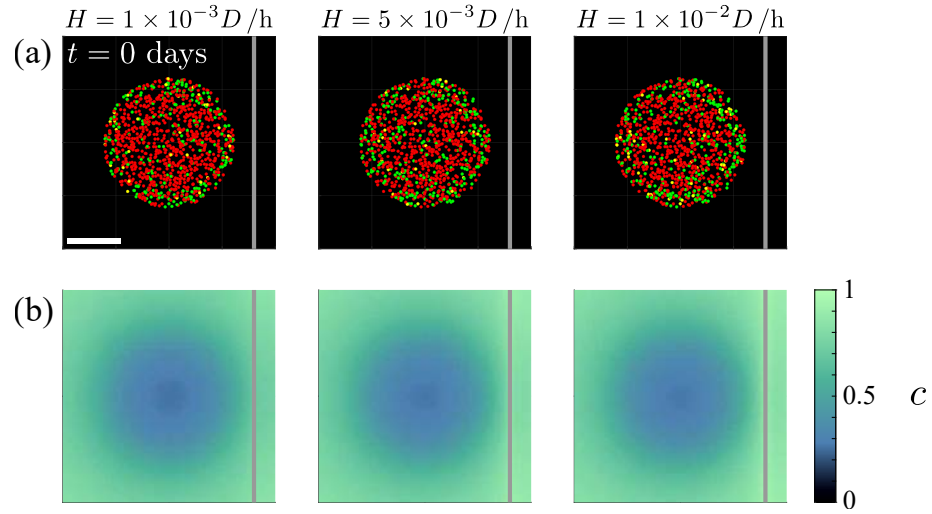


Figure 3.18: Initial equatorial spheroid and nutrient profile slices for spheroid growth with non-uniform nutrient conditions. (a) Visualisations of the spheroid equator with and without dead agents are identical, as the model does not initialise a dead population prior to spheroid formation. (b) The nutrient profile at $t = 0$ days showing the influence of increasing H . Scale bar is $200 \mu\text{m}$, and the location of the line source “blood vessel” is indicated with a grey line.

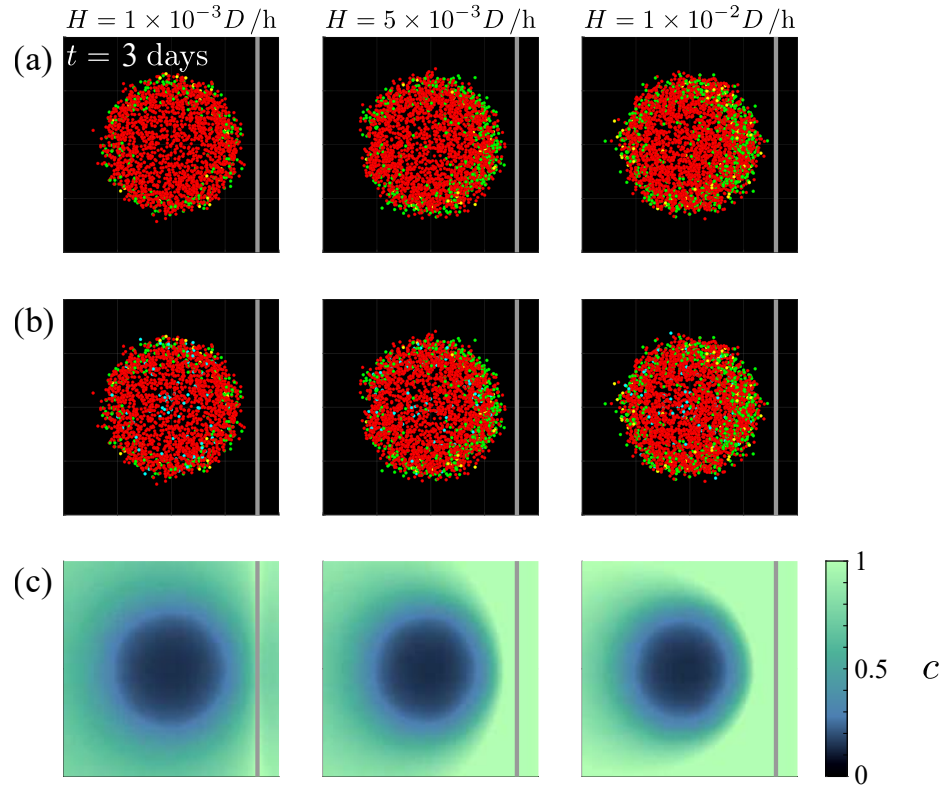


Figure 3.19: Spheroids grown with non-uniform nutrient delivery at $t = 3$ days, showing the effect of increasing H . The equatorial plane of the spheroid (a) without dead agents, (b) with dead agents, and (c) the corresponding nutrient profile. The scale bar is representative of $200 \mu\text{m}$, and the grey line indicates the line source.

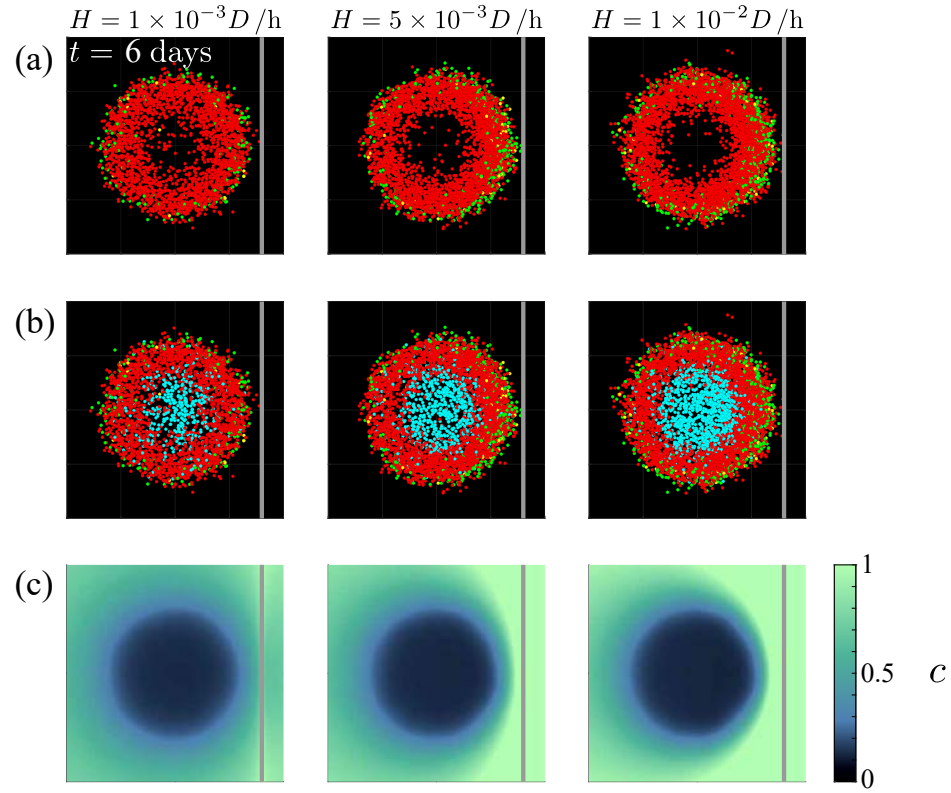


Figure 3.20: Spheroids grown with non-uniform nutrient delivery at $t = 6$ days, showing the effect of increasing H the spheroid at the equator (a) without dead agents, (b) with dead agents, and (c) the corresponding nutrient profile. Scale bar corresponds to $200 \mu\text{m}$, and the grey line indicates the line source.

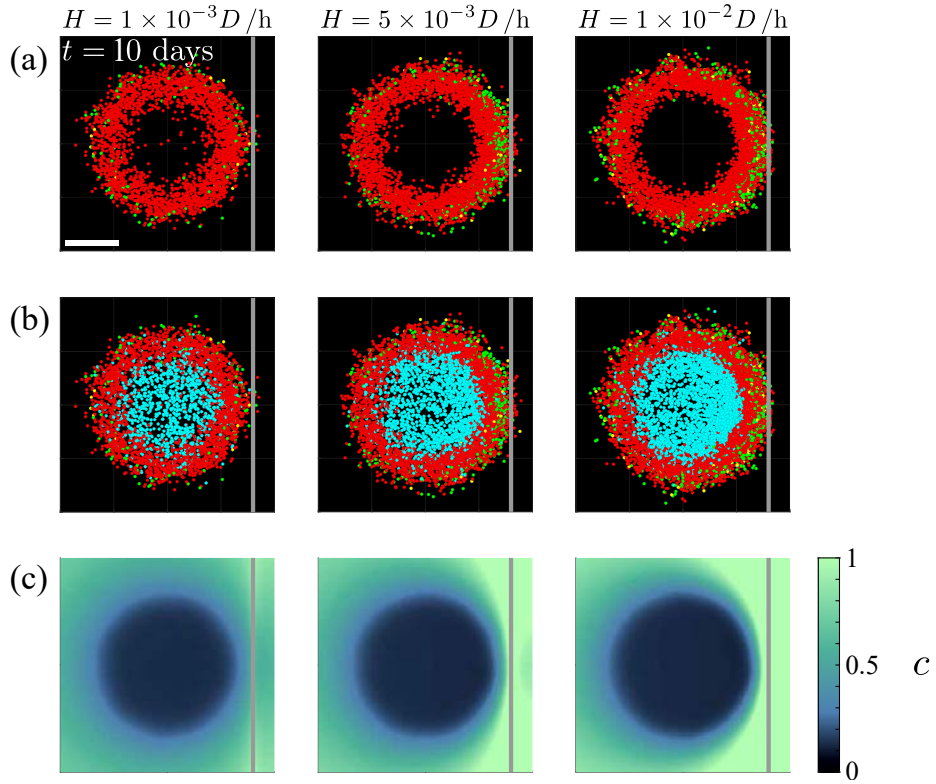


Figure 3.21: Spheroids grown under non-uniform nutrient delivery conditions at $t = 10$ days, demonstrating the effect of increasing H . The spheroid is visualised at the equator (a) without dead agents and (b) with dead agents. (c) The nutrient profile at the equator corresponding to the spheroid growth at $t = 10$ days. The scale bar represents $200 \mu\text{m}$, and the grey line indicates the location of the line source.

3.13 Conclusion

In this chapter, we present additional numerical and mathematical techniques, as well as experimental methods and results, to support the methodology, parameter choices, and results presented in Chapter 2. We demonstrate the numerical techniques for the estimates of the radii of each region for *in silico* data, and present a suite of numerical experiments to justify the choices of numerical parameters used in Table 2.1. A collection of experiments for estimating cell cycle progression rates, cell diameter estimates, and population count at the time of spheroid formation justify the choices of biological parameters used in Table 2.1. The algorithms for pseudo-code of the model and the calculation of agent density profiles are

described here as well. These mathematical and experimental techniques presented in this chapter provide support to the methods and results in Chapter 2.

Chapter 4

Conclusion

4.1 Summary

In this thesis, an IBM of 4D tumour spheroid growth with cell cycle labelling is formulated. Cell cycling, migration, and death are all regulated with the concentration of nutrient throughout the domain. A key outcome of the research is that the qualitative and quantitative experimental data can be matched with the IBM, and further detail that is unattainable in experimental assays can also be achieved with the model. Previous studies employ FUCCI labelling in 2D IBMs [20, 28, 30, 33], or IBMs of 4D tumour spheroids without FUCCI labelling [23, 24, 35]. This study consolidates these works to explicitly include FUCCI labelling into the modelling of 4D tumour spheroids.

In Chapter 2, a continuous-space, continuous-time IBM of 4D tumour spheroids with cell cycle indicators is presented. Unlike continuum models, the tumour spheroid evolution is modelled as the consequence of the collective behaviours of individual cells interacting with their environment. The environmental heterogeneity in the local nutrient concentration drives the heterogeneity in the cell cycle status, regions of necrosis, and the motilities of the agents. A key result of the research presented in Chapter 2 is the qualitative match between spheroids grown *in vitro* and *in silico* outcomes of the mathematical model. The formation and growth of the outer radius, arrested region, and necrotic core all exhibit the same qualitative behaviour *in vitro* and *in silico*. Demonstration of the model's biological fidelity then allows for the extraction and analysis of quantitative data that cannot be ascertained experimentally, such as nutrient concentration profiles and population counts, which further illuminate details about spheroid growth

in the model. These behaviours in the model arise from the biologically-inspired mechanisms of cell cycling, arrest, motility, and death. Chapter 2 is concluded by comparing the experimentally-accessible quantitative data – the radii of the spheroid, the arrested region, and the necrotic core – with estimates of these same quantities from the model, and showing that for a carefully selected parameter set, the IBM can reproduce quantitative experimental data. The code to reproduce key results in Chapter 2 are also made available on [GitHub](#). Chapter 2 shows that an IBM approach to modelling and reproducing the qualitative and quantitative evolution of tumour spheroids is effective, and also presents a method with which such a modelling approach can be constructed and extended.

Chapter 3 presents supporting information for Chapter 2. Numerical techniques for computational quantities are presented and demonstrated, as well as a collection of computational experiments that justify several numerical parameter choices. Additional supporting experiments are methodologically presented, and used to justify biological parameter choices. These additional methods and results complement the findings in Chapter 2.

4.2 Discussion

In this thesis, the growth of tumour spheroids is analysed through the development of an IBM, where behaviour on the individual scale determines the evolution of the spheroid as a whole. This individual-based model, under the assumption that nutrient diffusion is responsible for adjustments of cell behaviour, couples the availability of nutrient to the readiness of model agents to engage in cell cycling, migration, and death. The model assumes a quasi-steady state of nutrient, in congruence with previous studies and mathematical models of tumour spheroids with nutrient [10, 12, 24], an assumption that is appropriate due to the relative speed with which the nutrient diffuses in comparison with spheroid growth [10].

The validity of the IBM is investigated through a comparison of the mathematically-generated spheroids and spheroids grown *in vitro*. In doing so, we observe that the model captures the same qualitative behaviour of the typical *in vitro* tumour spheroid, particularly the rates of growth of the spheroid and the different regions that make up its composition. Numerical results in Chapter 3 demonstrate an appropriate choice of parameters for an accurate solution to the PDE is made; parameter choices with higher

temporal or spatial resolution (and therefore more accurate solutions) are indistinguishable from those selected for use in the model. Thus, we are confident in the accuracy of both the nutrient diffusion model and the spheroid evolution arising from behaviours coupled to the availability of this nutrient.

There are a variety of different human melanoma cell lines, each with their own properties [5]. While the IBM presented in this thesis utilises the metastatic human melanoma cell line WM793B, it is anticipated that the model is just as capable at matching the growth of spheroids with other cell lines and a variety of different initial conditions. However, we also anticipate that the parameter set required to achieve a match between the IBM and experimental assay may be drastically different; for example, the rates of progression through the stages of the cell cycle calculated in Chapter 3 may not necessarily be the same for other cell lines, as evidenced in [5]. Nonetheless, we anticipate the reproducing the growth of spheroids with other experimental conditions (cell line, initial population, etc.) would be possible under an appropriate parameter set.

4.3 Future Work

In this thesis, the modelling approach has been to work with the simplest possible mechanisms. Consequently, there are various avenues through which the IBM can be extended with future research.

In the model presented in this research, we implement a cell migration and proliferation mechanism where the direction of migration or proliferation is chosen at random, which is appropriate for our philosophy of using primarily simple modelling mechanisms. Previous IBMs studying 2D cell proliferation and migration have implemented a bias so that the cells can be more likely to move along a cell density gradient [21, 22, 32]. Although our simple assumption appears suitable for the data, it is possible to apply a proliferation and migration bias along the gradient of the 3D cell density or even nutrient concentration. This bias could be used to drive the spheroid growth in place of random proliferation and migration. Another extension of this approach could be to apply a mechanism of cell-to-cell mechanical forces. Similarly to [24], a mechanical force that mimics cell adhesion and repulsion can be implemented to improve the biological application of the model. In general, accounting for interaction behaviours between cells in the model would be a natural avenue of extension for the

IBM in this thesis.

In constructing the model, spheroid growth and cell behaviours are regulated by a single diffusible nutrient. This choice seems reasonable for our experimental data, which does not indicate that multiple, highly distinct species of nutrients play major roles in the spheroid's evolution. If, however, future experimental results indicate that a single diffusible nutrient species would be insufficient to adequately reproduce *in vitro* spheroid growth and nutrient profiles, the IBM framework is adaptable and can be modified to include new nutrients. Alternatively, the diffusion of a disruptive or cytotoxic cancer treatment drug could be implemented in tandem with the nutrient diffusion. The resulting interaction between the cells, nutrient, and drug could then become a focal point of investigation.

Each of these potential extensions to the IBM could readily be implemented and possibly lead to better qualitative or quantitative matches to experimental data. However, such an approach requires caution, as each new extension must involve an increase in the number of unknown parameters in the model. The IBM in this thesis uses a minimal model to avoid issues with parameter identifiability. However, the flexible construction of the IBM makes modifying it to include new extensions, such as those suggested here, a straightforward task, should future works determine that a minimal model is insufficient.

The model could also be refined through a thorough parameter estimation exercise. Here, tumour spheroid growth is modelled with carefully selected parameters, but future computation could analyse and estimate these parameter values and work towards a more rigorous parameter estimate assessment. In engaging in this task, it is important to consider that, like many discrete models, the IBM is less computationally efficient than a continuum model [18]. This presents an inherent barrier to parameter estimation exercises. However, a meticulous approach to estimating the model parameters would be a valuable direction of extension to this research.

This thesis demonstrates the potential of IBM approaches to reproducing the evolution behaviour of 4D tumour spheroids. The findings in this research show that both qualitative and quantitative experimental spheroid evolution can be reproduced by the with IBMs that explicitly include fluorescent cell cycle labelling, and the methodology can be further extended to include many more biological functions. Further opportunities to investigate the modelling potential of IBMs to tumour spheroids can be found in extending the scope of the IBM presented in this thesis.

Bibliography

- [1] Lazzari G, Couvreur P, Mura S, 2017. Multicellular tumor spheroids: a relevant 3D model for the *in vitro* preclinical investigation of polymer nanomedicines. *Polymer Chemistry*, **8**:4947–4969. doi: [10.1039/C7PY00559H](https://doi.org/10.1039/C7PY00559H). [1](#), [12](#)
- [2] Spoerri L, Beaumont KA, Anfosso A, Haass NK, 2017. Real-time cell cycle imaging in a 3D cell culture model of melanoma. *Methods in Molecular Biology*, **1612**:401–416. doi: [10.1007/978-1-4939-7021-6_29](https://doi.org/10.1007/978-1-4939-7021-6_29). [1](#), [12](#), [33](#), [51](#)
- [3] Nunes AS, Barris AS, Costa EC, Moreira AF, Correia IJ, 2018. 3D tumor spheroids as *in vitro* models to mimic *in vivo* human solid tumors resistance to therapeutic drugs. *Biotechnology and Bioengineering*, **116**:206–226. doi: [10.1002/bit.26845](https://doi.org/10.1002/bit.26845). [1](#), [12](#)
- [4] Minchinton AI, Tannock IF, 2006. Drug penetration in solid tumours. *Nature Reviews Cancer*, **6**:583—592. doi: [10.1038/nrc1893](https://doi.org/10.1038/nrc1893). [1](#), [4](#)
- [5] Haass NK, Beaumont KA, Hill DS, Anfosso A, Mrass P, Munoz MA, Kinjyo I, Weninger W, 2014. Real-time cell cycle imaging during melanoma growth, invasion, and drug response. *Pigment Cell & Melanoma Research*, **27**:764–776. doi: [10.1111/pcmr.12274](https://doi.org/10.1111/pcmr.12274). [1](#), [4](#), [5](#), [12](#), [13](#), [17](#), [27](#), [33](#), [51](#), [74](#)
- [6] Pampaloni F, Reynaud EG, Stelzer EHK, 2007. The third dimension bridges the gap between cell culture and live tissue. *Nature Reviews Molecular Cell Biology*, **8**:839–845. doi: [10.1038/nrm2236](https://doi.org/10.1038/nrm2236). [1](#)
- [7] Lin RZ, Chang HY, 2008. Recent advances in three-dimensional multicellular spheroid culture for biomedical research. *Biotechnology Journal*, **3**:1172–1184. doi: [10.1002/biot.200700228](https://doi.org/10.1002/biot.200700228). [1](#), [4](#), [5](#)

- [8] Mehta G, Hsiao AY, Ingram M, Luker GD, Takayama S, 2012. Opportunities and challenges for use of tumor spheroids as models to test drug delivery and efficacy. *Journal of Controlled Release*, **164**:192–204. doi: [10.1016/j.jconrel.2012.04.045](https://doi.org/10.1016/j.jconrel.2012.04.045). 1, 4, 5, 12
- [9] Kuang Y, Nagy JD, Eikenberry SE, 2016. *Introduction to Mathematical Oncology*. Chapman & Hall, Boca Raton, 1st edition. 1, 2, 5
- [10] Greenspan HP, 1972. Models for the growth of a solid tumor by diffusion. *Studies in Applied Mathematics*, **51**:317–340. doi: [10.1002/sapm1972514317](https://doi.org/10.1002/sapm1972514317). 2, 14, 17, 18, 73
- [11] McElwain DLS, Ponzo PJ, 1977. A model for the growth of a solid tumor with non-uniform oxygen consumption. *Mathematical Biosciences*, **35**:267–279. doi: [10.1016/0025-5564\(77\)90028-1](https://doi.org/10.1016/0025-5564(77)90028-1). 2, 14
- [12] Ward JP, King JR, 1997. Mathematical modelling of avascular-tumour growth. *Mathematical Medicine and Biology*, **14**:39–69. doi: [10.1093/imammb/14.1.39](https://doi.org/10.1093/imammb/14.1.39). 2, 14, 17, 73
- [13] Byrne HM, Chaplain MAJ, 1995. Growth of nonnecrotic tumors in the presence and absence of inhibitors. *Mathematical Biosciences*, **130**:151–181. doi: [10.1016/0025-5564\(94\)00117-3](https://doi.org/10.1016/0025-5564(94)00117-3). 2
- [14] Byrne HM, King JR, McElwain DLS, Preziosi L, 2003. A two-phase model of solid tumour growth. *Applied Mathematics Letters*, **16**:567–573. doi: [10.1016/S0893-9659\(03\)00038-7](https://doi.org/10.1016/S0893-9659(03)00038-7). 2
- [15] Jiang Y, Pjesivac-Grbovic J, Cantrell C, Freyer JP, 2005. A multiscale model for avascular tumour growth. *Biophysical Journal*, **89**:3884–3894. doi: [10.1529/biophysj.105.060640](https://doi.org/10.1529/biophysj.105.060640). 2
- [16] Leedale J, Herrmann A, Bagnall J, Fercher A, Papkovsky D, Séé V, Bearon RN, 2014. Modeling the dynamics of hypoxia inducible factor-1 α (HIF-1 α) within single cells and 3D cell culture systems. *Mathematical Biosciences*, **258**:33–43. doi: [10.1016/j.mbs.2014.09.007](https://doi.org/10.1016/j.mbs.2014.09.007). 2, 14
- [17] Grimes DR, Kelly C, Bloch K, Partridge M, 2014. A method for estimating the oxygen consumption rate in multicellular tumour spheroids. *Journal of the Royal Society Interface*, **11**:20131124. doi: [10.1098/rsif.2013.1124](https://doi.org/10.1098/rsif.2013.1124). 2, 14, 25

- [18] Michel T, Fehrenbach J, Lobjois V, Laurent J, Gomes A, Colin T, Poignard C, 2018. Mathematical modelling of the proliferation gradient in multicellular tumour spheroids. *Journal of Theoretical Biology*, **458**:133–147. doi: [10.1016/j.jtbi.2018.08.031](https://doi.org/10.1016/j.jtbi.2018.08.031). 2, 5, 75
- [19] Sakaue-Sawano A, Kurokawa H, Morimura T, Hanyu A, Hama H, Osawa H, Kashiwagi S, Fukami K, Miyata T, Miyoshi H, et al., 2008. Visualizing spatiotemporal dynamics of multicellular cell-cycle progression. *Cell*, **132**:487–498. doi: [10.1016/j.cell.2007.12.033](https://doi.org/10.1016/j.cell.2007.12.033). 4, 12
- [20] Vittadello ST, McCue SW, Gunasingh G, Haass NK, Simpson MJ, 2019. Mathematical models incorporating a multi-stage cell cycle replicate normally-hidden inherent synchronization in cell proliferation. *Journal of the Royal Society Interface*, **16**:20190382. doi: [10.1098/rsif.2019.0382](https://doi.org/10.1098/rsif.2019.0382). 4, 5, 12, 72
- [21] Binny RN, James A, Plank MJ, 2016. Collective cell behaviour with neighbour-dependent proliferation, death and directional bias. *Bulletin of Mathematical Biology*, **78**:2237–2301. doi: [10.1007/s11538-016-0222-9](https://doi.org/10.1007/s11538-016-0222-9). 4, 5, 74
- [22] Browning AP, McCue SW, Binny RN, Plank MJ, Shah ET, Simpson MJ, 2018. Inferring parameters for a lattice-free model of cell migration and proliferation using experimental data. *Journal of Theoretical Biology*, **437**:251–260. doi: [10.1016/j.jtbi.2017.10.032](https://doi.org/10.1016/j.jtbi.2017.10.032). 4, 5, 18, 32, 74
- [23] Mao X, McManaway S, Jaiswal JK, Patel PB, Wilson WR, Hicks KO, Bogle G, 2018. An agent-based model for drug-radiation interactions in the tumour microenvironment: hypoxia-activated prodrug SN30000 in multicellular tumour spheroids. *PLoS Computational Biology*, **14**:e1006469. doi: [10.1371/journal.pcbi.1006469](https://doi.org/10.1371/journal.pcbi.1006469). 4, 5, 14, 19, 72
- [24] Bull JA, Mech F, Quaiser T, Waters SL, Byrne HM, 2020. Mathematical modelling reveals cellular dynamics within tumour spheroids. *PLoS Computational Biology*, **16**:e1007961. doi: [10.1371/journal.pcbi.1007961](https://doi.org/10.1371/journal.pcbi.1007961). 4, 5, 14, 19, 22, 72, 73, 74
- [25] Jin W, Spoerri L, Haass NK, Simpson MJ, 2021. Mathematical model of tumour spheroid experiments with real-time cell cycle imaging.

- Bulletin of Mathematical Biology*, **83**:1–23. doi: [10.1007/s11538-021-00878-4](https://doi.org/10.1007/s11538-021-00878-4). 5, 14, 24
- [26] Murphy RJ, Browning AP, Gunasingh G, Haass NK, Simpson MJ, 2021. Designing and interpreting 4D tumour spheroid experiments. *bioRxiv preprint*. doi: [10.1101/2021.08.18.456910](https://doi.org/10.1101/2021.08.18.456910). To appear, *Communications Biology*. 5, 14, 20, 22, 29, 31
- [27] Saitou T, Imamura T, 2015. Quantitative imaging with Fucci and mathematics to uncover temporal dynamics of cell cycle progression. *Development, Growth Differentiation*, **58**:6–15. doi: [10.1111/dgd.12252](https://doi.org/10.1111/dgd.12252). 5
- [28] Simpson MJ, Jin W, Vittadello ST, Tambyah TA, Ryan JM, Gunasingh G, Haass NK, McCue SW, 2018. Stochastic models of cell invasion with fluorescent cell cycle indicators. *Physica A: Statistical Mechanics and its Applications*, **510**:375–386. doi: [10.1016/j.physa.2018.06.128](https://doi.org/10.1016/j.physa.2018.06.128). 5, 72
- [29] Bae H, Go YH, Kwon T, Sung BJ, Cha HJ, 2019. A theoretical model for the cell cycle and drug induced cell cycle arrest of FUCCI systems with cell-to-cell variation during mitosis. *Pharmaceutical Research*, **36**:1–13. doi: [10.1007/s11095-019-2570-2](https://doi.org/10.1007/s11095-019-2570-2). 5
- [30] Carr MJ, Simpson MJ, Drovandi C, 2021. Estimating parameters of a stochastic cell invasion model with fluorescent cell cycle labelling using approximate Bayesian computation. *Journal of the Royal Society Interface*, **18**:20210362. doi: [10.1098/rsif.2021.0362](https://doi.org/10.1098/rsif.2021.0362). 5, 14, 72
- [31] Breckling B, 2002. Individual-based modelling potentials and limitations. *The Scientific World Journal*, **2**:1044–1062. doi: [10.1100/tsw.2002.179](https://doi.org/10.1100/tsw.2002.179). 5, 6
- [32] Browning AP, Jin W, Plank MJ, Simpson MJ, 2020. Identifying density-dependent interactions in collective cell behaviour. *Journal of the Royal Society Interface*, **17**:20200143. doi: [10.1098/rsif.2020.0143](https://doi.org/10.1098/rsif.2020.0143). 5, 74
- [33] Vittadello ST, McCue SW, Gunasingh G, Haass NK, Simpson MJ, 2018. Mathematical models for cell migration with real-time cell cycle dynamics. *Biophysical Journal*, **114**:1241–1253. doi: [10.1016/j.bpj.2017.12.041](https://doi.org/10.1016/j.bpj.2017.12.041). 5, 72

- [34] Ortmann B, Druker J, Rocha S, 2014. Cell cycle progression in response to oxygen levels. *Cellular and Molecular Life Sciences*, **71**:3569–3582. doi: [10.1007/s00018-014-1645-9](https://doi.org/10.1007/s00018-014-1645-9). 5
- [35] Ruiz-Arrebola S, Tornero-López AM, Guirado D, Villalobos M, Lallena AM, 2020. An on-lattice agent-based Monte Carlo model simulating the growth kinetics of multicellular tumor spheroids. *Physica Medica*, **77**:194–203. doi: [10.1016/j.ejmp.2020.07.026](https://doi.org/10.1016/j.ejmp.2020.07.026). 5, 72
- [36] Beaumont KA, Mohana-Kumaran N, Haass NK, 2014. Modelling melanoma *in vitro* and *in vivo*. *Healthcare*, **2**:27–46. doi: [10.3390/healthcare2010027](https://doi.org/10.3390/healthcare2010027). 12, 27
- [37] Landman KA, Please CP, 2001. Tumour dynamics and necrosis: surface tension and stability. *Mathematical Medicine and Biology*, **18**:131–158. doi: [10.1093/imammb/18.2.131](https://doi.org/10.1093/imammb/18.2.131). 14
- [38] Browning AP, Sharp JA, Murphy RJ, Gunasingh G, Lawson B, Burrage K, Haass NK, Simpson MJ, 2021. Quantitative analysis of tumour spheroid structure. *eLife*, **10**:e73020. doi: [10.7554/eLife.73020](https://doi.org/10.7554/eLife.73020). 14, 20
- [39] Codling EA, Plank MJ, Benhamou S, 2008. Random walk models in biology. *Journal of the Royal Society Interface*, **5**:813–834. doi: [10.1098/rsif.2008.0014](https://doi.org/10.1098/rsif.2008.0014). 14, 18
- [40] Mallet DG, De Pillis LG, 2006. A cellular automata model of tumor-immune system interactions. *Journal of Theoretical Biology*, **239**:334–350. doi: [10.1016/j.jtbi.2005.08.002](https://doi.org/10.1016/j.jtbi.2005.08.002). 14
- [41] Ghaffarizadeh A, Heiland R, Friedman SH, Mumenthaler SM, Macklin P, 2018. PhysiCell: An open source physics-based cell simulator for 3-D multicellular systems. *PLoS Computational Biology*, **14**:e1005991. doi: [10.1371/journal.pcbi.1005991](https://doi.org/10.1371/journal.pcbi.1005991). 14, 18
- [42] Cooper FR, Baker RE, Bernabeu MO, Bordas R, Bowler L, Bueno-Orovio A, Byrne HM, Carapella V, Cardone-Noott L, Cooper J, et al., 2020. Chaste: cancer, heart and soft tissue environment. *Journal of Open Source Software*, **5**:1848. doi: [10.21105/joss.01848](https://doi.org/10.21105/joss.01848). 14, 18
- [43] Brown PJ, Green JEF, Binder BJ, Osborne JM, 2021. A rigid body framework for multicellular modeling. *Nature Computational Science*, **1**:754–766. doi: [10.1038/s43588-021-00154-4](https://doi.org/10.1038/s43588-021-00154-4). 14

- [44] Vipond O, Bull JA, Macklin PS, Tillmane U, Pugh CW, Byrne HM, Harrington HA, 2021. Multiparameter persistent homology landscapes identify immune cell spatial patterns in tumors. *Proceedings of the National Academy of Sciences of the United States of America*, **118**:e2102166118. doi: [10.1073/pnas.2102166118](https://doi.org/10.1073/pnas.2102166118). 14
- [45] Flegg A, Jennifer, Nataraj N, 2019. Mathematical modelling and avascular tumour growth. *Resonance*, **24**:313–325. doi: [10.1007/s12045-019-0782-8](https://doi.org/10.1007/s12045-019-0782-8). 14
- [46] Gillespie DT, 1977. Exact stochastic simulation of coupled chemical reactions. *The Journal of Physical Chemistry*, **81**:2340–2361. doi: [10.1021/j100540a008](https://doi.org/10.1021/j100540a008). 15
- [47] Weisstein EW, 2021. Sphere point picking. mathworld – A Wolfram web resource. <https://mathworld.wolfram.com/SpherePointPicking.html>. (Accessed: December 2021). 16
- [48] Simpson MJ, Landman KA, Hughes BD, 2010. Cell invasion with proliferation mechanisms motivated by time-lapse data. *Physica A: Statistical Mechanics and its Applications*, **389**:3779–3790. doi: [10.1016/j.physa.2010.05.020](https://doi.org/10.1016/j.physa.2010.05.020). 16, 18, 50
- [49] Johnston ST, Simpson MJ, Plank MJ, 2013. Lattice-free descriptions of collective motion with crowding and adhesion. *Physical Review E*, **88**(062720). doi: [10.1103/PhysRevE.88.062720](https://doi.org/10.1103/PhysRevE.88.062720). 18
- [50] Mueller-Klieser W, 1984. Method for the determination of oxygen consumption rates and diffusion coefficients in multicellular spheroids. *Biophysical Journal*, **46**:343–348. doi: [10.1016/S0006-3495\(84\)84030-8](https://doi.org/10.1016/S0006-3495(84)84030-8). 19
- [51] Mueller-Klieser W, Freyer JP, Sutherland R, 1986. Influence of glucose and oxygen supply conditions on the oxygenation of multicellular spheroids. *British Journal of Cancer*, **53**:345–353. doi: [10.1038/bjc.1986.58](https://doi.org/10.1038/bjc.1986.58). 19
- [52] Carlsson J, Acker H, 1988. Relations between pH, oxygen partial pressure and growth in cultured cell spheroids. *International Journal of Cancer*, **42**:715–720. doi: [10.1002/ijc.2910420515](https://doi.org/10.1002/ijc.2910420515). 19

- [53] Treloar KK, Simpson MJ, 2013. Sensitivity of edge detection methods for quantifying cell migration assays. *PLoS One*, **8**:e67389–e67389. doi: [10.1371/journal.pone.0067389](https://doi.org/10.1371/journal.pone.0067389). 20
- [54] Browning AP, Murphy RJ, 2021. Image processing algorithm to identify structure of tumour spheroids with cell cycle labelling. *Zenodo*. doi: [10.5281/zenodo.5121093](https://doi.org/10.5281/zenodo.5121093). 20, 34, 37, 38
- [55] Spoerri L, Tonnessen-Murray CA, Gunasingh G, Hill DS, Beaumont KA, Jurek RJ, Chauhan J, Vanwalleghem GC, Fane ME, Daignault-Mill SM, et al., 2021. Phenotypic melanoma heterogeneity is regulated through cell-matrix interaction-dependent changes in tumor microarchitecture. *bioRxiv preprint*. doi: [10.1101/2020.06.09.141747](https://doi.org/10.1101/2020.06.09.141747). 24
- [56] Miniaev MV, Belyakova MB, Kostiuk NV, Leshchenko DV, Fedotova TA, 2013. Non-obvious problems in Clark electrode application at elevated temperature and ways of their elimination. *Journal of Analytical Methods in Chemistry*, **2013**:249752. doi: [10.1155/2013/249752](https://doi.org/10.1155/2013/249752). 25
- [57] Langan LM, Dodd NJF, Owen SF, Purcell WM, Jackson SK, Jha AN, 2016. Direct measurements of oxygen gradients in spheroid culture system using electron parametric resonance oximetry. *PLoS One*, **11**:e0149492. doi: [10.1371/journal.pone.0149492](https://doi.org/10.1371/journal.pone.0149492). 25
- [58] Varia MA, Calkins-Adams DP, Rinker LH, Kennedy AS, Novotny DB, Fowler WC, Jr, Raleigh JA, 1998. Pimonidazole: a novel hypoxia marker for complementary study of tumor hypoxia and cell proliferation in cervical carcinoma. *Gynecologic Oncology*, **71**:270–277. doi: [10.1006/gyno.1998.5163](https://doi.org/10.1006/gyno.1998.5163). 27
- [59] Simpson MJ, Baker RE, Vittadello ST, Maclaren OJ, 2020. Practical parameter identifiability for spatio-temporal models of cell invasion. *Journal of the Royal Society Interface*, **17**:20200055. doi: [10.1098/rsif.2020.0055](https://doi.org/10.1098/rsif.2020.0055). 31, 32
- [60] Hoek KS, Schlegel NC, Brafford P, Sucker A, Ugurel S, Kumar R, Weber BL, Nathanson KL, Phillips DJ, Herlyn M, et al., 2006. Metastatic potential of melanomas defined by specific gene expression profiles with no BRAF signature. *Pigment Cell Research*, **19**:290–302. doi: [10.1111/j.1600-0749.2006.00322.x](https://doi.org/10.1111/j.1600-0749.2006.00322.x). 33

- [61] Smalley KSM, Contractor R, Haass NK, Kulp AN, Atilla-Gokcumen GE, Williams DS, Bregman H, Flaherty KT, Soengas MS, Meggers E, et al., 2007. An organometallic protein kinase inhibitor pharmacologically activates p53 and induces apoptosis in human melanoma cells. *Cancer Research*, **67**:209–217. doi: [10.1158/0008-5472.CAN-06-1538](https://doi.org/10.1158/0008-5472.CAN-06-1538). 33
- [62] Smalley KSM, Contractor R, Haass NK, Nathanson KL, Medina CA, T. FK, Herlyn M, 2007. Ki67 expression levels are a better marker of reduced melanoma growth following MEK inhibitor treatment than phospho-ERK levels. *British Journal of Cancer*, **96**:445–449. doi: [10.1038/sj.bjc.6603596](https://doi.org/10.1038/sj.bjc.6603596). 33, 34
- [63] Spoerri L, Gunasingh G, Haass NK, 2021. Fluorescence-based quantitative and spatial analysis of tumour spheroids: a proposed tool to predict patient-specific therapy response. *Frontiers in Digital Health*, **3**:1–19. doi: [10.3389/fdgth.2021.668390](https://doi.org/10.3389/fdgth.2021.668390). 33, 34
- [64] Cold Spring Harbor Laboratory Press, 2018. Antibody dilution buffer (Abdil) protocol. doi: [10.1101/pdb.rec103978](https://doi.org/10.1101/pdb.rec103978) (Accessed: December 2021). 33
- [65] Binder BJ, Simpson MJ, 2015. Spectral analysis of pair-correlation bandwidth: application to cell biology images. *Royal Society Open Science*, **2**:140494. doi: [10.1098/rsos.140494](https://doi.org/10.1098/rsos.140494). 37, 58
- [66] Crank J, 1975. *The Mathematics of Diffusion*. Clarendon Press, Oxford, 2nd edition. 40
- [67] Mathworks, 2021. MATLAB `ode45`. <https://www.mathworks.com/help/matlab/ref/ode45.html>. (Accessed: December 2021). 40
- [68] Mathworks, 2021. MATLAB `gmres`. <https://www.mathworks.com/help/matlab/ref/gmres.html>. (Accessed: December 2021). 42, 56
- [69] Mathworks, 2021. MATLAB `mldivide`. <https://au.mathworks.com/help/matlab/ref/mldivide.html>. (Accessed: December 2021). 44
- [70] ThermoFisher Scientific, 2021. CelltrackerTM. <https://www.thermofisher.com/order/catalog/product/C34565>. (Accessed: December 2021). 50

- [71] Schindelin J, Arganda-Carreras I, Frise E, Kavning V, Longair M, Pietzsch T, Preibisch S, Rueden C, Saalfeld S, Schmid B, et al., 2012. Fiji: an open-source platform for biological-image analysis. *Nature Methods*, **9**:676–682. doi: [10.1038/nmeth.2019](https://doi.org/10.1038/nmeth.2019). **50**, 53